



Recent advances in development of nanostructured photodetectors from ultraviolet to infrared region: A review



P.V. Karthik Yadav ^a, B. Ajitha ^b, Y. Ashok Kumar Reddy ^{a,*}, Adem Sreedhar ^{c, **}

^a Department of Physics, Indian Institute of Information Technology, Design and Manufacturing, Kancheepuram, Off Vandalur-Kelambakkam Road, Chennai, 600127, India

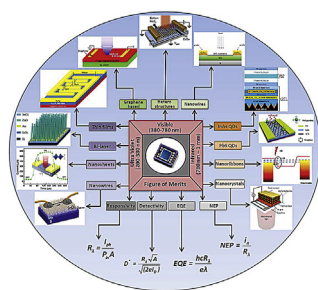
^b Division of Physics, School of Advanced Sciences, Vellore Institute of Technology (VIT), Vandalur - Kelambakkam Road, Chennai, 600127, India

^c Department of Physics, Gachon University, 1342 Seongnamdaero, Sujeong-gu, Seongnam-si, Gyeonggi-do, 461701, Republic of Korea

HIGHLIGHTS

- Systematically classified the photodetector materials based upon their spectral absorbance.
- Basic mechanism and prominent figures of merit of photodetectors are explained.
- The dependence of PD performance on various nanostructures are discussed.
- Most recent advancements in photodetectors are addressed by expound of their problems.

GRAPHICAL ABSTRACT



ARTICLE INFO

Article history:

Received 18 January 2021

Received in revised form

10 March 2021

Accepted 30 March 2021

Available online 12 April 2021

Handling Editor: Derek Muir

Keywords:

Photodetector

Ultra-violet

Visible

Infrared

Nanostructure

ABSTRACT

Herein, we aim to evaluate the photodetector performance of various nanostructured materials (thin films, 2-D nanolayers, 1-D nanowires, and 0-D quantum dots) in ultraviolet (UV), visible, and infrared (IR) regions. Specifically, semiconductor-based metal oxides such as ZnO, Ga₂O₃, SnO₂, TiO₂, and WO₃ are the majority preferred materials for UV photodetection due to their broad band gap, stability, and relatively simple fabrication processes. Whereas, the graphene-based hetero- and nano-structured composites are considered as prominent visible light active photodetectors. Interestingly, graphene exhibits broad band spectral absorption and ultra-high mobility, which derives graphene as a suitable candidate for visible detector. Further, due to the very low absorption rate of graphene (2%), various materials have been integrated with graphene (rGO-CZS, PQQ-rGO, N-SLG, and GO doped PbI₂). In the case of IR photodetectors, quantum dot IR detectors prevails significant advantage over the quantum well IR detectors due to the 0-D quantum confinement and ability to absorb the light with any polarization. In such a way, we discussed the most recent developments on IR detectors using InAs and PbS quantum dot nanostructures. Overall, this review gives clear view on the development of suitable device architecture under prominent nanostructures to tune the photodetector performance from UV to IR spectral regions for wide-band photodetectors.

© 2021 Elsevier Ltd. All rights reserved.

1. Introduction

In the past two decades, we have witnessed tremendous development in material science and nanotechnology, which has

* Corresponding author.

** Co-corresponding author.

E-mail addresses: akreddy111@gmail.com (Y.A. Kumar Reddy), ademsuva@gmail.com (A. Sreedhar).

been leading to strengthening of nanoelectronics technology (Khomutov et al., 2003). Specifically, various novel composite materials have been replaced traditional materials due to their drastic effect on our environment and poor device performance. In this viewpoint, researchers have been adopted various experimental techniques to constitute the novel materials under essential nanoscale structures, including nanowires, quantum dots, nanobelts, and thin films (Wang et al., 2020a; Ponraj et al., 2016). For this, strategic of fabrication methods including magnetron sputtering, electron beam evaporation, chemical vapor deposition (CVD), electrochemical and mechanical exfoliation, chemical etching, pulsed laser deposition (PLD), and spray pyrolysis have been paid great attention due to the potential high surface to volume ratio and stability with fewer defects (Zeng et al., 2012; Xia et al., 1999; Liu et al., 2005).

Because of the enriched physical and chemical properties, the nanostructures have emerged as attractive materials in the field of nanoelectronics, energy, optoelectronics, photocatalysis, sensors, drug delivery, biomedicine, lasers, and flexible technology (Wang, 2007; Laurenti et al., 2019; Cheng et al., 2017). In this era of modernization, most of the electronic devices directly or indirectly associated with the light interaction in various applications. For example, many diseases have been treated under powerful light exposures (lasers). In this point of view, photodetectors (PDs) have attracted considerable attention, which can effectively detect and measure the incident light. Specifically, photodetector technology practically applied in (i) ultra-violet (UV) region for ozone sensing, pollution detection, gas sensors, and flame detection, (ii) visible (Vis) region for energy, fiberoptic communications, video imaging, and artificial vision, and (iii) infrared (IR) region for bio-medical imaging, defence, space telescopes, and meteorology.

It is well-known that wide range of materials has been used for the PDs application including metal oxides, transition metal halides and perovskites. It is to be highlighted that if the composite materials integrated with different nanostructures, the sensitivity of the device can be greatly improved. Therefore, it is necessary to develop and explore the suitability of selective material for improved photodetector performance. In recent years, nanosheets of WO_3 PD are sensitive to UV light (365 nm) with responsivity of 293 A/W (Liu et al., 2015). On the other hand, WO_3 nanowires showed sensitive to visible light (404 nm) and produced the responsivity about 19 A/W (Wang et al., 2020b). Therefore, the reliability of PDs performance depends on key aspects, which including band gap, crystallinity, and particle size. In addition, thin film PDs have also been developed under good responsivity, which can be easily scalable for mass production. However, their response time is lagging due to the poor charge carrier mobility. Moreover, flexible PDs technology is emerging in smart phones, wearable technology, smart watches, and electronic tattoos. For this, ultra-thin materials are necessary with high efficiency (De Fazio et al., 2016). Typically, nanostructured materials are favored for the development of photodetector technology due to their attractive electronic properties, photo sensitivity, high charge carrier mobility, and flexible nature (Zhang et al., 2020). Therefore, various PDs based on vivid nanostructures (nanowires, nanorods, and quantum dots) have been developed as IR photodetectors to enhance the response speed and as well as to achieve superior figure of merits. Hence, this review summarizes the accomplishments of current PDs technology based on different nanostructures and also provides constructive discussion and challenges faced.

Based on the above spectral detectivity, photodetectors have been classified into three major categories (UV, Vis, and IR photodetectors) (Zhai et al., 2009). In recent years, concise applicability of emerging UV, Vis and IR photodetectors in various fields systematically represented in Fig. 1(a). Thus, photodetector performance

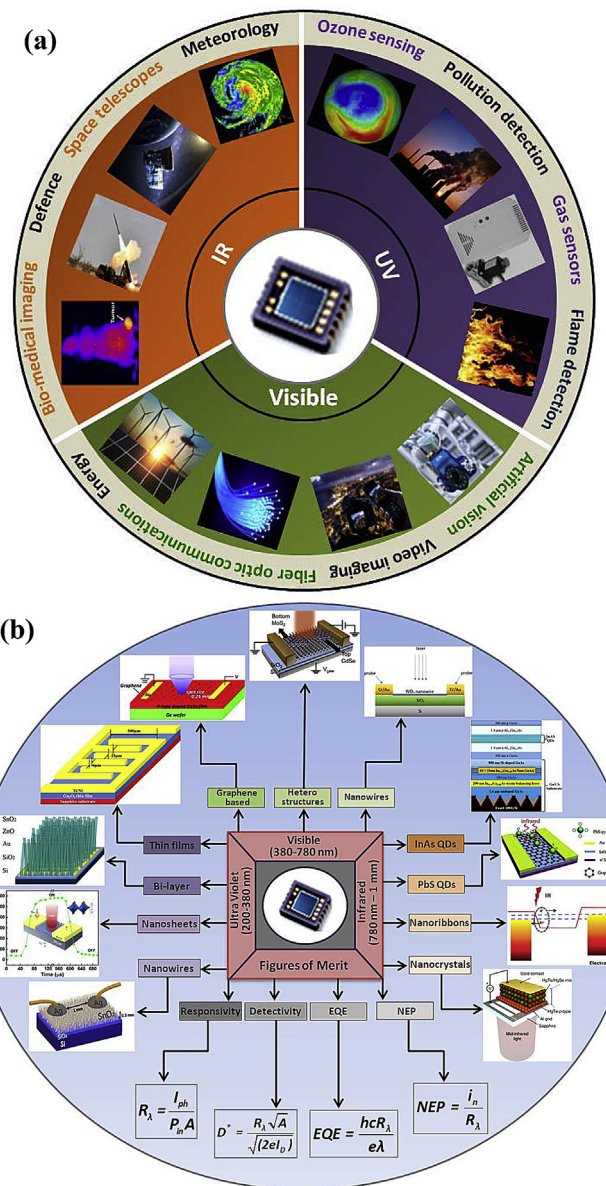


Fig. 1. Schematic outline of (a) applications and (b) review presentation on UV, visible, and IR photodetectors.

renders its applicability in various fields. Therefore, we divided the review paper into three major sections, which bring the simplicity of UV, visible, and IR photodetectors performance. Specifically, we have highlighted modern advancements on photodetector technology (UV, Vis, and IR regions) by considering the progressive categorization of material composition under spectral selectivity. The overall gist of the present review is illustrated in the Fig. 1(b). In particular, we tried to reveal the spectral absorption based on the device architecture such as thin films, nanosheets, nanowires, nanocrystals, and quantum dots towards superior photodetector performance.

1.1. Photodetector mechanism

Photodetectors emerged as a sensor of incident light, which mainly used to convert the incident photon energy into electrical signal. Typically, the sensing capacity of incident radiation can be greatly estimated by measuring the current or voltage signal

generated in the device. Thus, there is immense interest on the development of various photodetectors. Until now, many researchers reported various photodetector mechanisms enabled in the UV, Vis and IR regions. Therefore, it is necessary to develop the strategic device architecture under various composite materials to improve the sensing of incident light. In such a way, achieving superior photoresponsivity and photodetector sensing mechanism primarily related to the photoconductive, photogating, and photovoltaic effects.

1.1.1. Photoconductive effect

Photoconduction process is one of the important features to develop the high-performance photoconductors. Generally, the structure of photoconductor contains two metal-electrode contacts at both ends of the semiconductor, which establishes the ohmic-contact between semiconductor and metal-electrode. Thus, this device architecture illustrates the advantage of photoconduction mechanism by absorbing the incident light. As a result, electron-hole pair generation and separation can be effectively facilitated under electrons transfer from semiconductor to one end of electrode and holes to another end of electrode. However, superior photocurrent generation and separation of charge carriers are directly proportional to the applied potential. Moreover, photocurrent generation also depend on the charge carrier mobility and lifetime of the developed semiconductor. It should be noted that the photoconduction mechanism is predominantly seen in metal-semiconductor-metal (M-S-M) structured PDs. The M-S-M PDs consists of a simple planar structure with interdigitized electrodes, which can be easily integrated with other components in the optoelectronic circuits. In addition to that, M-S-M PDs provide less transit times for photogenerated charge carriers and possess high sensitivity. Accordingly, development of strategic approaches is necessary to develop the metal-semiconductor-metal (M-S-M) based PDs.

1.1.2. Photogating effect

Furthermore, photogating effect is also a unique case of photoconductive effect. Previous reports presented two kinds of photogating effect on graphene flakes dispersed into ZnO nanotubes and CsPbCl₃–Cs₄PbCl₆ perovskite films (Huang et al., 2020; Zhu et al., 2020a). In the first concept of mechanism, photogenerated electrons or holes can be trapped at the surface adsorbents or by the defect levels. While the other kind of photogenerated charge carriers (electrons or holes) circulates multiple times within the device and generate photocurrent in the circuit. In another kind of mechanism, charge carriers generate on the surface of adsorbents. Also, one kind of charge carriers diffuses into the material and contributes to current generation. The common concept in both cases is surface adsorbents acts as a gate, which stimulates the photocurrent generation. The regime of photogating and photoconducting effects is difficult to differentiate during the photodetector performance because of both phenomena happen in the same device.

1.1.3. Photovoltaic effect

A typical photovoltaic effect can be mainly observed during the formation of PN, NPN, PNP, and at metal-semiconductor interfaces. Therefore, the device architecture provides work function difference, charge carrier gradient, and Schottky junctions. These features lead to the formation of built-in electric field at the junction. As a result, photogenerated electrons and holes can be effectively separated. This phenomenon allows successful nonlinear current-voltage (I–V) characteristics. Specifically, the output is either photocurrent or photovoltage. Considering the above effective photogenerated charge carrier separation under built-in electric

field results in short-circuit current (I_{sc}) during closed circuit. On the other hand, separation of opposite charge carriers on either side allows for successful photovoltage (V_{oc}) generation.

1.2. Prominent figures of merit

It is well known that prominent features for superior photodetector performance are responsivity, detectivity, noise equivalent power, and external quantum efficiency. This means that the importance of figures of merit can be illustrated irrespective of film thickness, active area of the material, mechanism, architecture, and working conditions.

In order to quantify the photocurrent generation per unit of illuminating radiation, responsivity of the photodetector is the key parameter. The photoresponsivity (R_λ) is the ratio between photocurrent generation and incident light energy. The following expression ensures the responsivity of the photodetector (Omnes et al., 2007),

$$R_\lambda = \frac{I_{ph}}{P_{in}A} \quad (1)$$

where, I_{ph} , P_{in} , and A are photocurrent generation, power density of incident light, and effective area of the photo-active material, respectively.

To explain the minimum amount of illumination power required to produce a signal to noise ratio (SNR) of 1 at 1 Hz of bandwidth, noise equivalent power (NEP) is the perfect tool. The following equation represents NEP of the photodetector (Omnes et al., 2007),

$$NEP = \frac{i_n}{R_\lambda} \quad (2)$$

where, i_n is the noise current and R_λ is the responsivity. It should be highlighted that better photodetector performance can be achieved at reduced NEP value. According to the equation (2), NEP is directly proportional to the noise current, which is mainly associated with the dark current. Overall, simultaneous achievement of suppressed dark currents and higher responsivity configures less NEP.

To study the impact of structural and material integration on photodetector performance, detectivity (D^*) is also an essential parameter. Moreover, it is anticipated to enhance the overall photodetector performance. Specifically, two main factors such as noise developed and normalized SNR performance of the device can be revealed. Considering the above features, detectivity can be estimated by using the following expression (Omnes et al., 2007),

$$D^* = \frac{\sqrt{A\Delta f}}{NEP} \quad (3)$$

At low short noise conditions detectivity can be written as,

$$D^* = \frac{R_\lambda \sqrt{A}}{\sqrt{(2eI_D)}} \quad (4)$$

where, Δf , e , and I_D are bandwidth, electronic charge, and dark current respectively.

In addition to the above key features, external quantum efficiency (EQE) is also a prominent factor. The EQE can be defined as ratio between number of electron-hole pairs (contributed for photocurrent generation) and total number of electron-hole pairs produced (by absorbing the incident light). The following expression is used to determine the EQE of photodetector (Omnes et al., 2007),

$$EQE = \frac{hcR_\lambda}{e\lambda} \quad (5)$$

where, h is the planks constant and λ is the wavelength of the incident light. To study the impact of various nanostructures on the enhancement of photodetector performance (responsivity, detectivity, noise equivalent power, and external quantum efficiency), we explored the photodetector performance in UV, visible and IR region. Considering the above features, we extracted the superior photodetector performance of various materials in UV, Vis and IR regions.

2. Progress on UV photodetectors

Photodetection in UV region draws undivided extension due to its ability in diverse applications: (i) flame and radiation detection to take preventive measures, (ii) astronomical studies and secured space communications, (iii) environmental and biological studies, (iv) chemical analysis for screening, and (v) optical communications (vi) missile plume detection etc. In particular, typical UV radiation categorized into four main spectral regions such as UV-A (400 nm–320 nm), UV-B (320 nm–280 nm), UV-C (280 nm–200 nm), and far UV (200 nm–10 nm) (Ren et al., 2013). It should be highlighted that UV light (< 280 nm) cannot penetrate into the earth's atmosphere. Interestingly, previous studies show that most of the UV light reaching the atmosphere falls under UV-A category. Thus, detection of UV-A radiation detection become prominent (Reddy et al., 2019a,b; Yamada et al., 2019; Yadav et al., 2019; Wang et al., 2019; Yadav et al., 2021). Over a period of time wide range of materials such as perovskites, silicon derivatives, metal halides, transition metal dichalcogenides, and metal oxides have been developed to detect the UV light (Li et al., 2020; Shi et al., 2016; Ahmadi et al., 2017; Mu et al., 2017; Tian et al., 2015). Specifically, Si, SiC, diamond-based, nitride-based, transitional metal oxides, and metal di-chalcogens used to detect the UV radiation (Konstantatos et al., 2010, 2012). For better UV photodetection and extensive period, photomultiplier tubes were utilized under compact size.

Nowadays, significant research is focusing on the fabrication of portable and highly sensitive UV detectors due to its rapid usage in microelectronic devices. Owing to the significant capability of UV absorption, several silicon-based materials have been extensively used in various fields. However, silicon exhibits a bandgap of 1.1 eV, which make it to absorb visible radiation. To avoid that, several layers of high-pass optical filters have been strategically introduced, which suggests the expensive device fabrication process. Particularly, insertion of filters possesses relatively high noise generation (Chen et al., 2020a). Therefore, transition metal oxides, SiC, and AlGaN alloys especially attractive for UV photodetection under its chemically and thermally stable nature. Interestingly, bandgap of above all materials falls under UV light, suggesting that we can avoid the usage of high-pass optical filters (Chen et al., 2020a). In another direction, metal oxide-based semiconductors such as ZnO, SnO₂, Ga₂O₃, WO₃, and TiO₂ established as an excellent UV photoactive material in optoelectronic devices. The above wide band gap metal oxide materials establish outstanding processing approaches such as ease fabrication, scalability, control over crystal orientations, uniformity, and reproducibility in the UV photodetector community. In such a way, all of the above features demonstrate that metal oxide semiconductors (ZnO, SnO₂, Ga₂O₃, WO₃, and TiO₂) can be widely used in highly sensitive UV photodetectors.

2.1. ZnO-based photodetectors

Among various metal oxide semiconductors, ZnO has been extensively studied and used in various applications (Khan et al., 2020; Saric et al., 2019; Shiau et al., 2020; Chauhan et al., 2020; Rabani et al., 2021). In particular, ZnO exhibit a wide bandgap (~3.2 eV) and n-type semiconductor behavior with exciton binding energy of ~60 meV (Pearson et al., 2003). Considering the wide bandgap, ZnO importance significantly aided for the improved UV absorption. Note that engineering of ZnO UV photodetectors also involves superior charge carrier generation (electron-hole pair) and separation. Driven by the above-mentioned constructive features, we here attempted to explore various device fabrication techniques to reveal superior UV photodetector performance. In this section, M-S-M structured Pd and Ti doped ZnO films have been demonstrated for better understanding the possibility of Schottky and ohmic contacts formation for superior UV photodetector performance.

The role of thermal evaporation and sol-gel deposition techniques has been highlighted to achieve superior UV photodetector properties of ZnO thin films under Schottky junction formation (Ali and Chakrabarti, 2012) In this study, a key factor for superior UV photodetector performance of ZnO thin films compared by considering the deposition techniques. The sol-gel derived ZnO thin film photodetectors exhibited superior responsivity (0.17 A/W) and EQE (62%) compared to the thermal evaporated ZnO (responsivity of 0.08 A/W and EQE of 23%). It is to be highlighted that sol-gel technique is a feasible route to realize the adsorption and desorption of H₂O and oxygen. Thus, sol-gel derived ZnO thin films have prevailed superior photodetector properties compared to the thermal evaporated samples.

Chemical bath deposition (CBD) method also guided to develop stable ZnO films. After that, UV photoconductive behavior of ZnO films (at 70 °C) studied under the precise M-S-M structure formation (Shaikh et al., 2016). Specifically, the ZnO deposition time can be modulated to improve the UV photodetector performance. Here, Ag metal used as electrode material. In this regard, the fabricated Ag/ZnO/Ag (M-S-M structure) device architecture exhibited superior photocurrent generation (113.83 μA) and responsivity (28.14 A/W) under UV light intensity ($\lambda = 365$ nm) of 1.8 μW/cm² at applied bias of 5 V. Moreover, as the dependence of CBD technique on ZnO thin film deposition, the photodetector stability and reversibility can be significantly improved with a rise time of 9 s and a fall time of 21 s. On the other hand, enhanced photoresponse attributed to the improved crystalline nature of ZnO films (as deposited for 7 h) and interconnected wire structured morphology. At higher deposition time, ZnO films peeled off easily. Considering the CBD technique and deposition time, it mean that superior charge carrier (electrons) transportation effectively observed at the metal-semiconductor interface.

Sol-gel technique is also beneficial for the fabrication of ZnO-based M-S-M Schottky barrier UV photodetectors (Ali et al., 2014). In this work, the photoresponse of pure ZnO, Pd doped ZnO, and Pd microplate embedded ZnO films have been compared, while Pd used as a Schottky-contact. Here, barrier-height and saturation current density of M-S-M photodiode were extracted using logarithmic reverse current dependence. The Pd metal microplates incorporated with ultra-thin ZnO films showed higher responsivity (0.33 A/W) and EQE (115%) under UV illumination (360 nm). Whereas undoped ZnO (0.15 A/W and 52%) and Pd–ZnO films (0.20 A/W and 70%) exhibited reduced responsivity and EQE respectively than compared to the Pd microplate embedded ZnO

films. The above results suggested that Pd microplate embedded ZnO exhibit superior UV photodetector under depletion region formation at the interface of microplates and semiconductor interface.

In another direction, simple spray pyrolysis technique was adopted to improve the UV photodetector performance of ZnO thin films under Ag metal as an electrode (Inamdar et al., 2014). Under forward and reverse bias conditions, I–V characteristics confirmed the ohmic-contact formation of between Ag metal and ZnO. It should be noted that UV photodetector performance of ZnO was completely under visible-blind. As a result, ZnO exhibited highest responsivity of ~788 A/W under 375 nm of UV illumination. Overall, superior photocurrent and photoresponse properties of ZnO mainly due to the highly crystalline nature of ZnO and intrinsic donor defects (oxygen vacancies and Zn interstitials). Such behavior also observed by the ZnO thin films developed by the CBD method (Shaikh et al., 2016).

In addition to the pure ZnO (Inamdar et al., 2014), researchers further focused on development of transition metal doped ZnO (Ti-doped ZnO) thin films by spray pyrolysis technique to investigate the UV detection properties (Shewale et al., 2015). Here, photodetector performance of pure and Ti-doped ZnO films systematically studied under Sn as a metal electrode contact, which developed the M-S-M structural configuration on both ZnO and Ti-doped ZnO samples. Accordingly, linear I–V characteristics of this M-S-M structure under forward and reverse bias confirmed the ohmic contacts between the metal (Sn) layers and semiconductor (Ti-doped ZnO). At selective bias voltage of 5 V, superior photocurrent generation of 112.68 μ A was observed for the Ti-doped ZnO under UV illumination ($\lambda = 365$ nm), which is higher than dark state (6.10 nA). At the same time, the responsivity was about 0.051 A/W under the light intensity of 2 mW/cm². In conclusion, it has been found that Ti metal doping significantly improved the charge carrier density in the ZnO, which yielded superior UV photodetector performance.

Low-cost solution processed method has been established to develop the ZnO nanowires for studying the UV photodetector performance (Ates et al., 2012). Single-walled carbon nanotubes (SWNT) layer was used as electrode onto the ZnO nanowires. Fig. 2(a) presents the schematic representation of SWNT thin films/ZnO nanowire photodetector. Here, various experimental studies conducted to reveal the relation between photodetector performance and nanowire density. These studies suggest that photocurrents were significantly improved by increasing the nanowire density and maximum photocurrent shown was 520 μ A under 365 nm of UV light. As a result, SWNT thin films/ZnO nanowire photodetector exhibited lower recovery time about 16 s (Fig. 2(b)), which is ascribed to the improved charge carriers. Unlike the other ZnO thin film photodetectors, transparent ZnO nanowires developed on flexible substrates exhibited stable UV photodetector performance even under different radii of curvature.

Among the above discussed ZnO based PDs, spray deposited ZnO thin film PDs (M-S-M structure) achieved superior responsivity about 788 A/W upon 375 nm UV illumination, compared to other ZnO based PDs. It was mainly due to the negligible dark currents under intrinsic donor defects, oxygen vacancies, and interstitial Zn. On the other hand, ZnO NWs were exhibited superior photocurrent about 520 μ A under UV illumination of 365 nm wavelengths and comparable responsivity of 0.15 A/W than other ZnO PDs. It should be highlighted that high surface to volume ratio of ZnO NWs resulting in higher photo absorption.

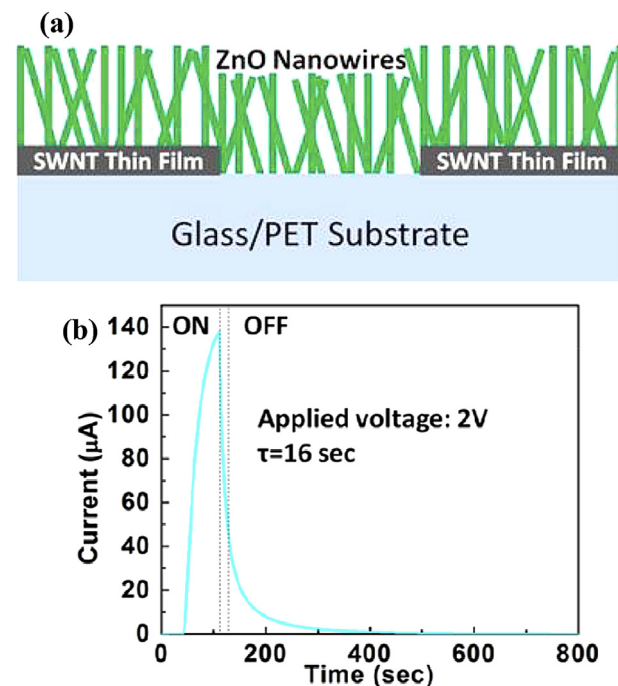


Fig. 2. Schematic depictions of (a) device structure of ZnO nanowire-based UV photodetector and (b) response and recovery current curve at an applied bias of 2 V of a ZnO nanowire (Ates et al., 2012).

2.2. *SnO₂*-based photodetectors

Apart from the ZnO, SnO₂ also found its importance in UV PDs application and it behaves like a transparent metal oxide semiconductor. It is generally agreed that SnO₂ exhibits chemically and thermally stable nature at atmospheric conditions (Wang et al., 2018). On the other hand, SnO₂ is highly transparent to the visible spectrum and reflects most of the IR radiation. Thus, SnO₂ is suitable for transparent heat reflective surfaces (Pandey et al., 2020). Due to its transparent nature, SnO₂ was vastly used in LCDs, LEDs, plasma display panels, and flat touch panels (Ramarajan et al., 2020). Apart from the above optoelectronic devices, SnO₂ also investigated in photocatalytic activity and active-anode material in Li-ion batteries (Zhang and Wang, 2020). In this section, we systematically discussed the development of SnO₂-based composites for enhancing the stability and overall UV photodetector performance.

Recently, SnO₂ nanowire networks have successfully synthesized using CVD technique, which followed the vapor-liquid-solid mechanism (de Araujo et al., 2020). Here, M-S-M based structure was demonstrated neither by expensive photolithography nor in a clean room atmosphere. Specifically, the photodetector performance of SnO₂ nanowire network studied under various excitation sources such as (i) UV lamp (2 mW/cm²) at wavelengths of 254 nm and 365 nm, (ii) white light (9.5 mW/cm²), and (iii) direct sun light (78.6 mW/cm²). Upon UV illumination, SnO₂ observed with superior photodetector performance with rise time (t_r) of 0.37 s and fall time (t_f) of 0.59 s at 5 V bias voltage. It has been found that rise time and fall time increased in the case of sun light ($t_r = 0.61$ s and $t_f = 0.55$ s) and white light ($t_r = 71.6$ s and $t_f = 131.5$ s) conditions. Apart from this, high sensitivity (>104) was obtained under UV

light compared to the outdoor measurements. It concluded that SnO_2 prevailed superior UV photodetector performance.

Similarly, vertically aligned SnO_2 NWs were successfully synthesized by glancing angle deposition (GLAD) method (Chetri et al., 2020). In this investigation, effect of annealing temperature (350°C , 550°C , 650°C , 750°C , and 900°C) on structural, optical, and electrical properties of SnO_2 NWs systematically studied. In such a way, the device fabricated at selective annealing temperature of 650°C achieved improved crystalline nature. Therefore, SnO_2 NWs annealed at 650°C achieved superior photodetector performance with maximum responsivity of 2.58 A/W and photodetectivity of $64.13 \times 10^{10} \text{ Jones}$ at $\lambda = 300 \text{ nm}$ of irradiance than other annealing temperatures. In a word, crystalline nature boosted the capacity of defect controlling, which results to the increase of charge carriers.

In addition to the above pure SnO_2 NWs (de Araujo et al., 2020; Chetri et al., 2020), SnO_2 -based heterojunction (ZnO/SnO_2) core-shell nano-rod arrays (CSNAs) developed using facile hydrothermal and chemical liquid deposition techniques (Fu et al., 2020). They highlighted the importance of localized excitons for recovery of near-band-edge transition. Therefore, $I_{\text{photo}}/I_{\text{dark}}$ ratio of ZnO/SnO_2 ensured 7.2×10^4 at 1 V, which was ~270 times higher than pure ZnO . Further, with the introduction of localized states in the ZnO/SnO_2 , ZnO/SnO_2 enhanced the photoresponse by means of responsivity (28.5 A/W) and specific detectivity ($2.9 \times 10^{14} \text{ Jones}$). It is also improved in mitigating the response time of ZnO/SnO_2 (8.7 s) compared to ZnO (45.0 s). On the other hand, recovery time of ZnO/SnO_2 (20.8 s) also decreased compared to ZnO (56.6 s) under nanocrystalline SnO_2 shell-layer development on ZnO .

In another direction, superior photodetector performance was achieved by developing the flexible hollow-sphere SnO_2 photodetector using water-oil interfacial assembling technique onto the polyethylene terephthalate (PET) substrate (Tian et al., 2013). Under specific hand-operable shadow mask, Cr/Au electrodes were deposited on the as-transformed SnO_2 hollow-sphere nanofilm. Fig. 3(a) represents the photodetector mechanism based on the

oxygen absorption and desorption for achieving the smooth transfer of charge carriers under UV illumination. The band to band charge carrier transition between the SnO_2 hollow spheres is presented in Fig. 3(b). The device performance was investigated both in vacuum and ambient atmosphere. Both dark and light currents were higher in the vacuum conditions due to the reduced gas pressure. The linear I–V curves of the device revealed the ohmic-contact formation. Moreover, the SnO_2 hollow sphere film device exhibits high sensitivity, stability and improved signal-to-noise ratio (SNR) about 300 times under the illumination of UV light of wavelength 320 nm at $45 \mu\text{W/cm}^2$ intensity. The enhanced sensitivity and SNR was attributed to the efficient photo-absorption by high surface to volume ratio SnO_2 hollow spheres. The spectroscopic photocurrent responds of the SnO_2 device is depicted in Fig. 3(c) at different incident wavelengths. The photocurrent was found to be 1.5 nA at 320 nm of illumination. Overall, the obtained results attest that SnO_2 is highly sensitive to the UV light.

From the above SnO_2 -based materials, ZnO/SnO_2 core shell NRs achieved superior photocurrents about 3.2 mA , which is 1000 times higher than pure SnO_2 NWs. It is to be highlighted that constructive interfacial interaction between ZnO and SnO_2 resulted improved photon absorption and photocurrent generation. On the other hand, SnO_2 nanospheres showed very low photocurrent about 1.5 nA . But, its dark to light photocurrent ratio was much higher, which is also compatible with the flexible technology.

2.3. Ga_2O_3 -based photodetectors

In addition to the ZnO and SnO_2 , Ga_2O_3 is also a promising transparent metal oxide semiconductor with a wide bandgap of $\sim 4.8 \text{ eV}$ (Chen et al., 2018). In such a way, Ga_2O_3 diversely used in the field of UV-optoelectronics, antireflective coatings, high-temperature sensors, and solar cells (Guo et al., 2019; Xu et al., 2020; Minami et al., 2013). Thus, we elaborately discussed the importance and recent advancements in the Ga_2O_3 -based UV

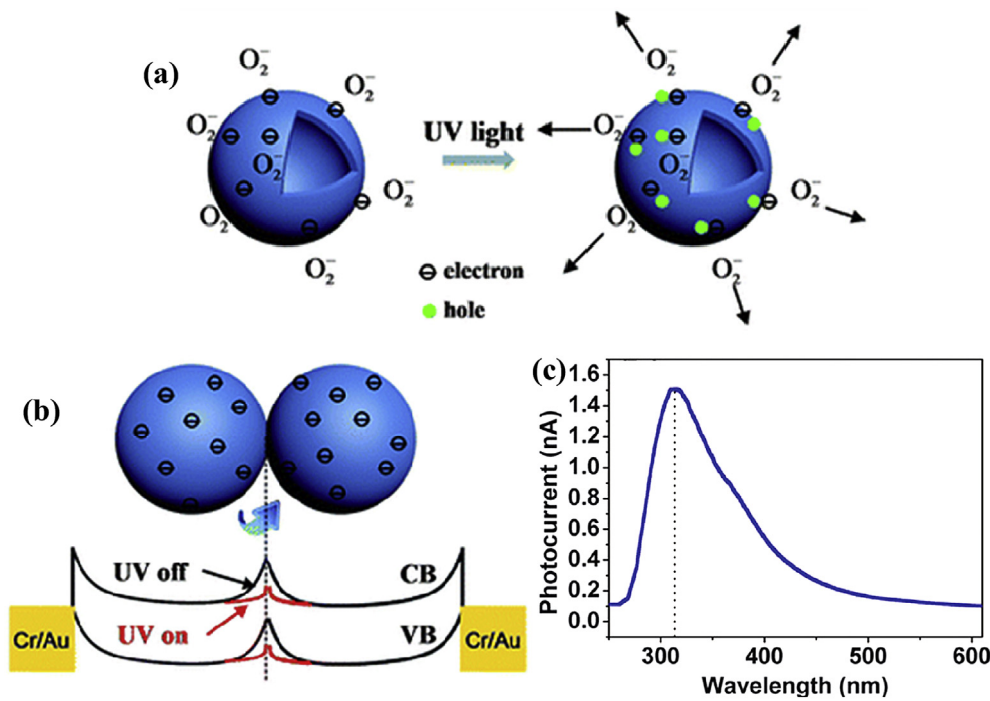


Fig. 3. Graphic representation of (a) oxygen-adsorption process under dark and oxygen-desorption process under UV-illumination of the SnO_2 hollow spheres, (b) sphere-to-sphere junction barrier for an electron transfer in the hollow sphere network, and (c) spectroscopic photocurrent responds of the device at different incident wavelengths (Tian et al., 2013).

photodetectors.

Amorphous Ga_2O_3 (α - Ga_2O_3) was synthesized at different deposition temperatures (RT-room temperature, 200 °C, 300 °C, 400 °C, and 500 °C) for achieving the solar-blind deep UV photodetector performance (Zhu et al., 2020b). In this study, higher oxygen vacancies have been developed at higher deposition temperatures, which resulted in improved responsivity, wider detection range, and longer photo-decay time. Specifically, α - Ga_2O_3 developed at selective deposition temperature of 500 °C exhibited superior photoresponsivity about 138 A/W compared to other temperatures of RT (1.46 A/W), 200 °C (16 A/W), 300 °C (25 A/W), and 400 °C (71 A/W). Overall, deposition temperature played a key role to improve the UV photodetector performance of α - Ga_2O_3 .

In addition to the α - Ga_2O_3 (Zhu et al., 2020b), highly-crystallized single β - Ga_2O_3 micro/nano-sheets were also studied to achieve superior UV photodetector performance under Schottky barrier formation (Zhong et al., 2015). Interestingly, β - Ga_2O_3 showed significant rectifying property under asymmetric contact formation at an open circuit voltage of 0.33 V and UV wavelength of 254 nm. In such a way, β - Ga_2O_3 achieved remarkable photodetector performance such as sensitivity (dark current of ~10 nA), R_λ (19.31 A/W), EQE (9427%), fast response time (about 20 ms), excellent stability and reversibility. All these features pave a potential path towards microwave device, high-speed integrated circuit, solar cells, and photo-switches formation.

In addition to the pure Ga_2O_3 , Mg-doped amorphous gallium oxide (Mg: GaO_x) films exhibited remarkable solar-blind UV photodetector (SBUV PD) performance (Zhang et al., 2019). Interestingly, Mg: GaO_x film highlighted with decrement in the trapping centers for achieving the improved photo-generated charge carriers. Specifically, Mg: GaO_x -based SBUV PD exhibited suppressed dark currents (48 pA), higher light-to-dark current ratio (~338 at -3 V bias voltage), and faster response (a decay time of 0.15 s) time. Thus, Mg-divalent ion dopant plays a key role in GaO_x to achieve the lower dark-current and quick response time.

Thin films of poly- Ga_2O_3 was developed using sputtering technique on *c*-plane sapphire substrate followed by the thermal annealing at 800 °C, 900 °C, 1000 °C, and 1100 °C (Hu et al., 2020). Later, Ti and Ni metal electrodes were developed on poly- Ga_2O_3 thin films. Consequently, M-S-M device structure was achieved as shown in Fig. 4(a). In particular, Ga_2O_3 thin films annealed at 1100 °C temperature showed less responsibility and photocurrent than the as deposited samples. This was due to recrystallization and diffusion of Al from the substrate into Ga_2O_3 films caused wide bandgap energy of 5.10 eV, which is higher than the incident UV energy to generate photocurrent. However, Ga_2O_3 films annealed at

1000 °C achieved remarkable responsivity of 20 μA/W, which was 500% higher than the Ga_2O_3 samples deposited at room RT (~7.5 μA/W) as shown in Fig. 4(b). Moreover, lower dark currents about 0.0033 nA (at bias voltage of 5 V) achieved at 1000 °C.

In summary, α - Ga_2O_3 based UV PDS showed superior responsivity of 138 A/W. It was mainly due to the high transparent nature of the amorphous Ga_2O_3 . Whereas Mg- GaO_x by showed responsivity of 0.14 A/W, which was quite lower due to the increased resistance. Here, Mg was used as a dopant in amorphous Ga_2O_3 to reduce the interstitial defects and oxygen vacancies. On the other hand, one-dimensional β - Ga_2O_3 nanobelts showed highest responsivity of 851 A/W than nanostructured single- Ga_2O_3 nanosheets with a responsivity of 19.31 A/W. overall, these results indicated that the better PD performance was produced by nanostructures of crystalline Ga_2O_3 films.

2.4. WO_3 -based photodetectors

In spite of the above encouraging UV photodetector performance of various metal oxides, tungsten trioxide (WO_3) is a transition metal oxide semiconductor with a bandgap of 3.2 eV (He et al., 2015). Primarily, the performance of WO_3 extensively studied in the field of electrochromic devices owing to its thermal and chemical stability. Thus, it has been used as dazzle-free mirrors in automobiles, variable reflection mirrors, and smart windows (Buch et al., 2016). It should be noted that WO_3 also provides structural transformation and non-stoichiometric phase transitions, which ensured its importance precisely in optoelectronic sensors and display systems (Siciliano et al., 2008; Jain et al., 2021). Thus, we explored the importance of UV photodetector performance of WO_3 and WO_3 -based materials.

Few-layered WO_3 nanosheets were successfully fabricated towards superior UV photodetector performance (Liu et al., 2015). Here, WO_3 nanosheets were synthesized by the CVD technique on the Si/SiO₂ substrate. Later, photolithography was used to develop the patterns and Cr/Au metal electrodes were deposited using e-beam deposition. Therefore, WO_3 nanosheets exhibited superior photoresponse (293 A/W) and EQE (997%) under UV light ($\lambda = 365$ nm). It is further established that the photocurrent generation under switching on and off cycles was quick and stable. Here, the $I_{\text{photo}}/I_{\text{dark}}$ ratio was observed with 2000, which expected to develop ultrafast WO_3 based optoelectronic devices.

As WO_3 nanosheets revealed very high responsivity under UV illumination, another group developed WO_3 monolayer by atomic layer deposition (ALD) onto the Si wafer to evaluate its UV PDs performance as shown in the (Hai et al., 2017a). Unlike the thin film

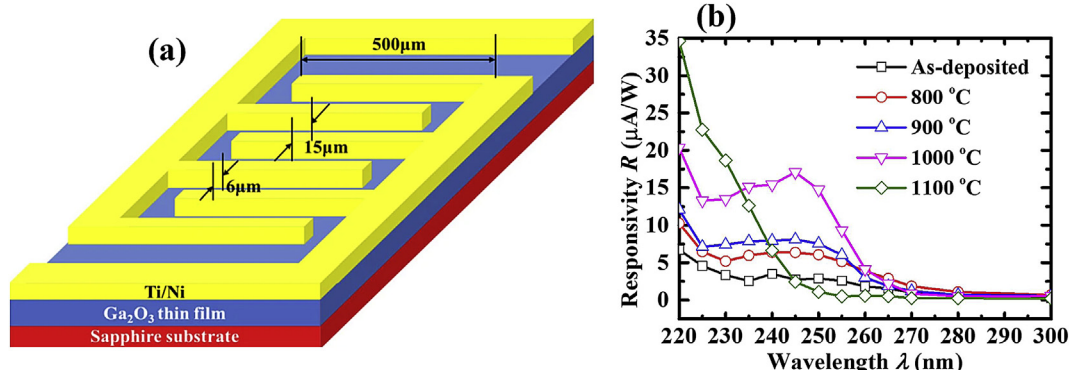


Fig. 4. Device structure representation of (a) M-S-M structured Ga_2O_3 -based UV photodetector (Hu et al., 2020) and (b) responsivity behavior as a function of incident wavelength (UV-light) for the poly-($\text{Al}_x\text{Ga}_{1-x}$) O_3 photodetectors at bias voltage of 5 V.

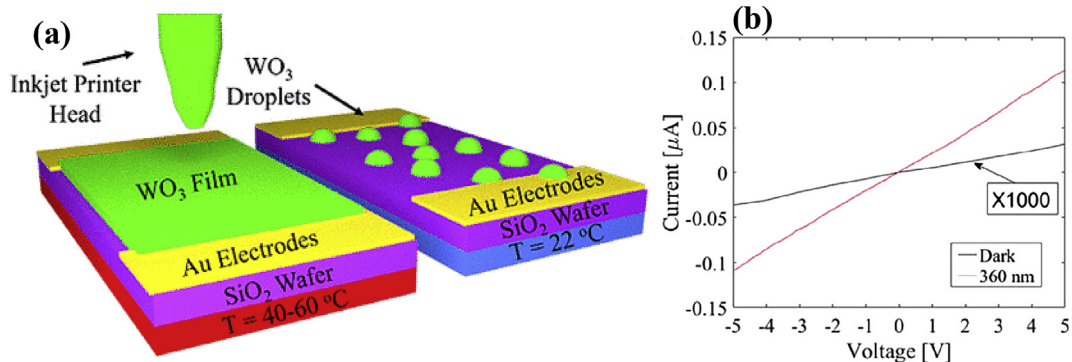


Fig. 5. (a) WO_3 photodetector fabricated through ink print on SiO_2/Si wafers with Au electrodes and (b) dark and photocurrent response at different bias voltages of WO_3 -based photodetector under UV-illumination (Cook et al., 2018).

based WO_3 PDs (Yadav et al., 2019), monolayer of WO_3 exhibited ultra-fast response (~2.5–2.7 ms) while maintaining long-term stability for about 250 cycles. The simple design of monolayer semiconductor oxide enhanced the dynamics of photon-semiconductor interactions without many losses due to the electron backscattering which is usually observed in multilayered nanostructures. In addition to this, ohmic-contact between the photoactive material and electrode as shown in also assisted in enhancing the photocurrent. Fig. 5(a) shows the inkjet printed WO_3 thin film developed onto the SiO_2 substrate based UV photodetectors and Fig. 5(b) exhibits the evidence of ohmic-contact between the electrode and photo-active material (Cook et al., 2018). Even though, both ink jet printed WO_3 thin films and ALD synthesized mono-layer of WO_3 consists of ohmic-contact, the mono-layer of WO_3 was exhibited the higher responsivity of 71.6 A/W than inkjet-printed WO_3 thin film (2.70 A/W). It was due to the efficient charge transfer by 2-D structured WO_3 device.

Implying a similar device concept, monolayer structured WO_3 demonstrated for revealing the photodetector performance in UV-A region with strategic functional capabilities (Hai et al., 2017b). It is important to note that the precise role of monolayer structured WO_3 achieved ultrafast photoresponse time (<40 μs) and photo-responsivity (~0.329 A/W). The above achieved response time was superior to the earlier reports on WO_3 -based UV photodetectors. Also, monolayer WO_3 responded quickly under UV-A light compared to most of the other 2-D ultrathin nanomaterial photodetectors. Specifically, monolayer structure certainly possesses quantum-confined effects and new functional opportunities to power the various optoelectronic devices. Because the monolayer WO_3 processes new path for the fabrication of highly flexible, inexpensive, and extremely sensitive photodetectors, it is reasonable to expect these types of UV photodetectors in industrialization and commercialization.

The popular M-S-M device structure is successfully synthesized by stacking the WO_3 nanospheres and WO_3 thin films on sapphire substrates (Lee et al., 2018). The dominant noise source of the M-S-M UV photodetector was flicker noise. The UV photodetector performance of M-S-M structured WO_3 nanospheres/ WO_3 thin film was higher than thin film structured WO_3 M-S-M photodetector. The above features determine the strength of high surface-to-volume ratio of WO_3 nanospheres. Accordingly, WO_3 nanosphere/ WO_3 thin film M-S-M device architecture (at a wavelength of 350 nm) achieved superior photoresponsivity (89.2 mA/W), noise equivalent power ($6.10 \times 10^{-11} \text{ W}$), and detectivity (5.19×10^9 Jones) compared to the M-S-M structured WO_3 thin film photodetector (photoresponsivity-20.7 mA/W, noise equivalent power-

$2.35 \times 10^{-10} \text{ W}$ and detectivity 1.34×10^9 Jones).

Building upon the above WO_3 based PDs, the pleasant surprise is that nanosheets showed excellent responsivity of 293 A/W, which was higher than that of other WO_3 based UV PDs discussed. In another creative study, few layers of WO_3 nanosheets outperformed the photodetector performance compared to the monolayered WO_3 . Experimental realization revealed that band gap of few layered WO_3 nanosheets confined to the UV region (365 nm), which stimulated the overall photodetector performance.

2.5. TiO_2 -based photodetectors

To prove the viability of TiO_2 on various applications, researchers focused on the photocatalysis, Li-ion batteries, solar cells, photodetectors, and self-cleaning surface coatings (Cho et al., 2021; Yan et al., 2017; Kment et al., 2017; Zheng et al., 2016; Patrocinio et al., 2014). It is particularly important to prove and understand the UV photodetector performance. We briefly note that TiO_2 is a transitional metal oxide, comes with a bandgap of (3.2 eV) and exhibits rutile, anatase, and brookite crystalline forms (Zhao et al., 2007). However, one must consider the chemical inertness, high photocatalytic activity, strong oxidizing power, endurance, non-toxicity, and low fabrication cost of TiO_2 (Hitosugi et al., 2010; Bera et al., 2018). Thus, TiO_2 also inspired by the excellent structural transformation and non-stoichiometric phase transitions, which safeguarded its importance in optoelectronic sensors and display systems. In the following discussion, we systematically discussed and examined the importance of TiO_2 -based UV photodetectors.

Nanocrystalline M-S-M structured $\text{Au}/\text{TiO}_2/\text{Au}$ thin films were fabricated by the sol-gel technique (Xue et al., 2007). The above device structures highlighted the importance of dark currents in the order of nA (1.9 nA) and photoresponsivity of 199 A/W under a wavelength of 260 nm (at 5 V bias voltage). Taken together, high responsivity being made by the existence of neutral photoconductor region and reduced Schottky barrier. The $\text{Au}/\text{TiO}_2/\text{Au}$ M-S-M structure showed defects trapped in the nanocrystal has been widely distributed. These widely distributed defects acted as the recombination centers, which were eventually resulted in the decrement of response time (rise time of 6 s and decay time of 15 s). Overall, all the above features (reduced recombination, defect trapping and lower response time) attributed to the improved crystalline nature of the TiO_2 nanocrystals.

Similar M-S-M device structure also studied on RF magnetron sputtered TiO_2 thin films (Caliskan et al., 2013). Here, Pt/Au metal electrode contacts used to develop the M-S-M device structure. With the development of M-S-M device structure, avalanche effect

and high electric field between the electrodes significantly influenced the exponential growth of dark current. As a result, M-S-M based photodetector helpful for the achieving the very low dark currents about 1.57 nA/cm^2 at 5 V. The results show that the TiO_2 M-S-M photodetector at specific bias voltage of 50 V and wavelength of 300 nm achieved the responsivity of 1.73 A/W . Also, the response time of the photodetector was measured under the rise and fall time of 7 s and 3 s, respectively. It can be attributed to the increased trap density existing in the as-deposited films and limited space between metal contacts and photo-active material.

To further study the importance of M-S-M structure, epitaxial TiO_2 thin films were deposited on LaAlO_3 single crystal substrates by RF sputtering technique (Xing et al., 2011). Here, Ag metal contacts were developed on the epitaxial TiO_2 layers and $\text{Ag/TiO}_2/\text{Ag}$ UV PD test device has been fabricated. Accordingly, the M-S-M based TiO_2 photodetector exhibited the superior responsivity of 3.63 A/W at a UV wavelength of 310 nm. In order to achieve the ohmic-contact behavior in M-S-M photodetector, it is necessary to use the high work function Ag metal as electrode. Because of ohmic-contact behavior, M-S-M structure proved reduced dark currents about 0.14 nA at a bias voltage of 10 V.

Implying a similar concept, high-quality TiO_2 epilayers were developed on the lattice-matched LaAlO_3 substrates at 500°C using pulsed laser deposition technique (Zhang et al., 2015). A prototype of M-S-M based $\text{Au/TiO}_2/\text{Au}$ UV-photodetector device was fabricated using Au as Schottky-contact. Here, the as-deposited TiO_2 thin film exhibited excellent visible-blind UV characteristics with an optical bandgap of 3.25 eV, signifying its potential in UV detection. As a result, this M-S-M based TiO_2 UV-photodetector device architecture had been proven as a high UV to visible rejection ratio of 10^5 under low dark-currents (0.25 pA at 5 V) and high responsivity (0.21 A/W) upon UV illumination of wavelength 270 nm. Such a low dark current value reveals the Schottky junction formation at the interface of metal/semiconductor.

Unlike the pure TiO_2 , another $\text{TiO}_2/\text{Ag}/\text{TiO}_2$ tri-layered structure fabricated using GLAD technique to realize the self-powered photodetector under dissimilar top electrodes (Ferhati et al., 2020). The optical activity of multilayered $\text{TiO}_2/\text{Ag}/\text{TiO}_2$ was first optimized using the genetic algorithm global optimization technique, where outstanding UV–Vis absorbance behavior was

achieved. Accordingly, the device responsivity significantly improved by 80% with extremely low dark-currents ($\sim 50 \text{ pA}$) compared to the traditional TiO_2 UV-PDs ($\sim 20 \mu\text{A}$). Bringing together, the optimized $\text{TiO}_2/\text{Ag}/\text{TiO}_2$ device exhibited outstanding UV responsivity of 0.2 A/W , detectivity of $5.3 \times 10^{13} \text{ Jones}$ and $I_{\text{on}}/I_{\text{off}}$ ratio of 137.2 dB , even under self-powered operating mode upon 365 nm monochromatic UV light illumination.

Considering the TiO_2 based UV photodetectors, TiO_2 nanocrystalline films ($\text{Au/TiO}_2/\text{Au}$) achieved remarkable responsivity (199 A/W) under the wavelength 260 nm of UV light. It was primarily due to the improved crystallinity and reduced Schottky barrier height. However, TiO_2 thin film and TiO_2 epilayer based PDs exhibited comparatively low responsivity of 3.63 A/W (310 nm) and 0.21 A/W (270 nm), respectively. Besides, the TiO_2 based materials raised its importance as a UV-A sensitive nature and preferred for environmental applications.

In the above sections, we have explored the strategic approaches to fabricate the UV photodetectors using various metal oxide semiconductors (ZnO , Ga_2O_3 , SnO_2 , TiO_2 , and WO_3). Specifically, experimental conditions such as deposition time, metal contacts and annealing temperature greatly devoted to achieving superior UV photodetector performance. By comparing the annealing temperature, Ga_2O_3 films annealed at 600°C achieved excellent responsivity of 138 A/W compared to the SnO_2 annealed at 500°C (2.58 A/W). Indeed, doping effect predominantly influenced the dark current of Pd doped ZnO and Mg doped Ga_2O_3 films. Especially, the flexibility of UV nanostructure photodetectors (nanowires and nanospheres) appeared to reduce the dark currents. But, the responsivity was low due to the increased recombination rate. However, the responsivity of the UV photodetector drastically increased to 28.5 A/W by introducing the bi-layer of ZnO/SnO_2 . It was due to the formation of optimized heterojunction interface and smooth flow of photogenerated charge carriers. Among all the metal oxides, WO_3 films deposited (CVD technique) achieved high responsivity (293 A/W) and $I_{\text{photo}}/I_{\text{dark}}$ ratio (2000). Overall, taking the benefits of optimized experimental conditions, appropriate doping element and developing of bi-layers significantly influenced the photodetector performance of WO_3 . Considering the above key features, we summarized the UV photodetector performance of various metal oxide semiconductors (ZnO , Ga_2O_3 ,

Table 1
Photodetector performance comparison under UV illumination with different semiconducting metal oxides.

Material	Methodology	Photocurrent (μA)	Responsivity (A/W)	Detectivity (Jones)	EQE (%)	Ref
ZnO	Sol-gel	1.35	0.17	—	62	(Ali and Chakrabarti, 2012)
ZnO	Chemical bath	113.8	0.33	—	115	Shaikh et al. (2016)
Pd–ZnO	Sol-gel	—	0.14	—	—	Ali et al. (2014)
ZnO	Spray pyrolysis	—	788	—	—	Inamdar et al. (2014)
Ti–ZnO	Spray pyrolysis	112.68	0.051	—	—	Shewale et al. (2015)
ZnO NW	Spin coating	520	—	—	—	Ates et al. (2012)
SnO ₂ NW	CVD	25	—	—	—	de Araujo et al. (2020)
SnO ₂ NW	GLAD	—	47.9	64.1×10^{10}	1.0×10^2	Chetri et al. (2020)
ZnO/SnO ₂	Hydrothermal	3.22×10^3	28.5	2.9×10^{14}	—	Fu et al. (2020)
SnO ₂ spheres	Interfacial assembling	1.5×10^{-3}	—	—	—	Tian et al. (2013)
Ga ₂ O ₃	RF sputtering	111	138	—	—	Zhao et al. (2020)
Ga ₂ O ₃	CVD	2.8	19.31	—	9.4×10^3	Zhong et al. (2015)
Mg:GaO _x	—	—	—	—	—	Zhang et al. (2019)
Ga ₂ O ₃	RF sputtering	12×10^{11}	20×10^{-6}	—	—	Hu et al. (2020)
WO ₃ NS	CVD	~25	293	—	9.9×10^2	Jain et al. (2021)
WO ₃ monolayer	ALD	15.1×10^3	71.6	—	1.13×10^4	Hai et al. (2017b)
WO ₃ monolayer	ALD	900	0.329	—	—	Hai et al. (2017c)
WO ₃ NS	VCCS	—	0.089	5.19×10^9	—	Lee et al. (2018)
TiO ₂	Sol-gel	2.3	199	—	—	Xue et al. (2007)
TiO ₂	RF sputtering	~1	1.73	—	—	Caliskan et al. (2013)
TiO ₂	RF sputtering	48	3.63	—	—	Xing et al. (2011)
TiO ₂	PLD	1.0	0.21	—	—	Zhang et al. (2015)
TiO ₂ /Ag/TiO ₂	GLAD	100	0.2	5.3×10^{13}	—	Ferhati et al. (2020)

SnO_2 , TiO_2 , and WO_3) in Table 1.

3. Research progress on visible photodetectors

Despite the significant advantage and importance of UV photodetectors based on wide band gap materials in field of environmental monitoring, flame detection and controlling, visible PDs also have numerous applications in the contemporary world of technology in the following aspects: (i) collision detectors for monitoring hurdles in driver bling spot, detectors for controlling air bags opening timings in usage in automotive technology and (ii) also in ultra-fast imaging technology. With the emergence of visible light photodetectors, it is essential to understand the visible light photodetector mechanism and performance to reach the current technological requirements. Primarily, previous reports on silicon and germanium based materials highly suitable for visible light photodetector performance due to its narrow bandgap (Kontantatos et al., 2007; Yang et al., 2017, 2018; Wang et al., 2014, 2015; Flemban et al., 2017; Xue et al., 2011; Siontas et al., 2019). It should be noted that visible light photodetectors exhibit higher response time, poor sensitivity, high dark current and relatively low EQE compared to UV photodetectors.

Interestingly, great efforts have been devoted on lead dihalide (LDH) and transition metal dichalcogenides to achieve the superior visible light response (Velusamy et al., 2015; Wu et al., 2016a; Zhang et al., 2016; Lin et al., 2015; Ramasamy et al., 2016). It should be noted that these materials are very susceptible to react with the environmental oxygen. However, PbI_2 and PbFI show excellent response under vacuum conditions (Ismail et al., 2019; Wei et al., 2017; Wang et al., 2017). Very recently (Shkir et al., 2019), reported cadmium zinc telluride (CZT) and indium-doped CZT (InCZT) single crystals-based visible light photodetectors with high responsivity. On the other hand, two-dimensional (2D) graphene (rich of carbon atoms) came into limelight. Thus, it has been used in numerous fields including solar cells, sensors, and optoelectronics. Indeed, graphene with packed carbon atoms exhibit superior mechanical strength, high electron conductivity, broad range spectral absorption, and ultra-high mobility (Falkovsky, 2008; Balandin, 2011; Papageorgiou et al., 2017; Neto et al., 2009). In the photodetector field, inherent structural stability describes the improved overall photodetector performance. Considering the above constructive features, we explored the importance of 2D graphene-based and other heterostructures towards visible light photodetector performance.

3.1. Graphene based visible photodetector

Recently, cadmium zinc selenide nanostructures and rGO were prepared separately and then mixed together as a solution in a Teflon beaker containing glass substrate. Then the CZS-rGO nanocomposite thin films were deposited on the substrate through hydrothermal-assisted chemical bath deposition technique for revealing the visible light photodetector performance (Mathew et al., 2020). Here, the authors investigated the photodetector performance under effective active area of 0.5 cm^2 , where silver paste was used as an electrode material. In this study, the device performance was significantly increased under selective rGO concentration of 2 wt%. The results showed that rGO-CZS achieved superior visible light responsivity (18.5 mA/W) and specific detectivity ($2.08 \times 10^{12} \text{ Jones}$). Most importantly, the rGO sheets included in this device contributed to superior charge carrier mobility, which eventually reduced the transit time. In a word, rGO-CZS represent the strength of visible light responsivity under the community of rGO sheets.

Novel perovskite quantum dots (PQDs) developed on rGO (PQD/rGO)

as a bi-layer revealed the visible photodetector performance (Chowdhury et al., 2020). Specifically, PQD/rGO structure describes the advantage of negatively charged functional groups present on the rGO surface for the diffusion of electron cloud, nucleation, and growth of PQDs on rGO. As a bilayer formation of PQD/rGO, desired charge transfer occurs from PQDs to rGO compared to the PQDs and rGO mixture as a thin film using spin coating or drop-casting method. The precise development of PQD-rGO exhibited high responsivity ($1.07 \times 10^3 \text{ A/W}$), detectivity ($1 \times 10^{13} \text{ Jones}$), and sharp switching in the visible region. Fig. 6(a) and (b) depict the schematic representation of GPQD-rGO photodetector and energy band alignment, which reveals the charge transfer from GPQD and rGO. Fig. 6(c) illustrates the transient photoresponse of GPQD-RGO superstructure under light illumination (442 nm) with On and Off conditions for one cycle. From the spectrum, fast photoresponse was observed with quick rise time (0.3 s) and fall time (0.3 s). As the PQDs normally grown on rGO, low responsivity was achieved due to the poor charge transfer at the interface. Therefore, the direct growth of PQDs on the rGO sheets could be adopted for development of stable visible light active 2-D photodetectors like transition metal halides and metal dichalcogenides.

Recently, investigation on gallium nitride (GaN) and nitrogen-doped single-layer graphene (N-SLG) heterostructures endeavored to reveal the visible photodetector performance (Sankaranarayanan et al., 2020). In this work, the GaN epilayer was deposited on N-SLG substrates using CVD technique. They selected Au as a metal contact, which associated for developing the M-S-M structured photodetector. Experimental results, further suggest that the M-S-M structure formation prevailed superior responsivity and detectivity in the range of $150\text{--}400 \text{ A/W}$ and $1.08 \times 10^{12}\text{--}2.89 \times 10^{12} \text{ Jones}$, respectively. Confirming the superior visible light response, the M-S-M structure further observed with the rising time and fall time of 10 ms and 25 ms, respectively. Overall, the GaN epilayer deposited on N-SLG substrate were highly prompt to the visible light with an improved charge carrier mobility and charge carrier generation.

Usually graphene oxide (GO) provides superior charge carrier mobility for further development in the visible light photodetector performance. In such a way, graphene oxide doped lead iodide (GO-PbI₂) studied for achieving the visible light photodetection performance under 532 nm (Sharma et al., 2020). In this study, PbI₂ nanorods/GO heterostructure was synthesized via microwave-assisted synthesis route. As the influence of GO doping, the photodetector performances of GO-PbI₂ such as R_s , EQE, and D* were significantly increased (0.182 A/W , 42%, and $1.79 \times 10^{11} \text{ Jones}$) compared to the pure PbI₂ (0.060 A/W , 14%, and $6.38 \times 10^{10} \text{ Jones}$). It is to be highlighted that the GO-PbI₂ mainly provides the trap centers at the interface, which filled under visible light illumination. It can be attributed to the superior charge carrier mobility of GO in the GO-PbI₂.

On the other hand, metallic (1T) configuration WSe₂ from transition metal dichalcogenides family also exhibited highly efficient visible photodetector performance with the integration of rGO (He et al., 2020). The nanostructures were systematically synthesized using modified-hydrothermal process. The results showed that rGO/WSe₂ achieved remarkable photodetector performance under improved (i) photocurrent generation by the 1T-configuration WSe₂ and (ii) charge carrier mobility of rGO, which proving efficient charge transfer at the interface of rGO/WSe₂. Accordingly, rGO/WSe₂ exhibited superior photoresponsivity (~105 A/W) compared to the pure WSe₂ (~89 A/W) under visible light of wave length 540 nm. In such a way, the time taken for light response of rising and decay were 0.001 s and 0.002 s respectively. Thus, the rapid raising and decay of photocurrents of rGO/WSe₂ describes the capability of improved electrical conductivity under

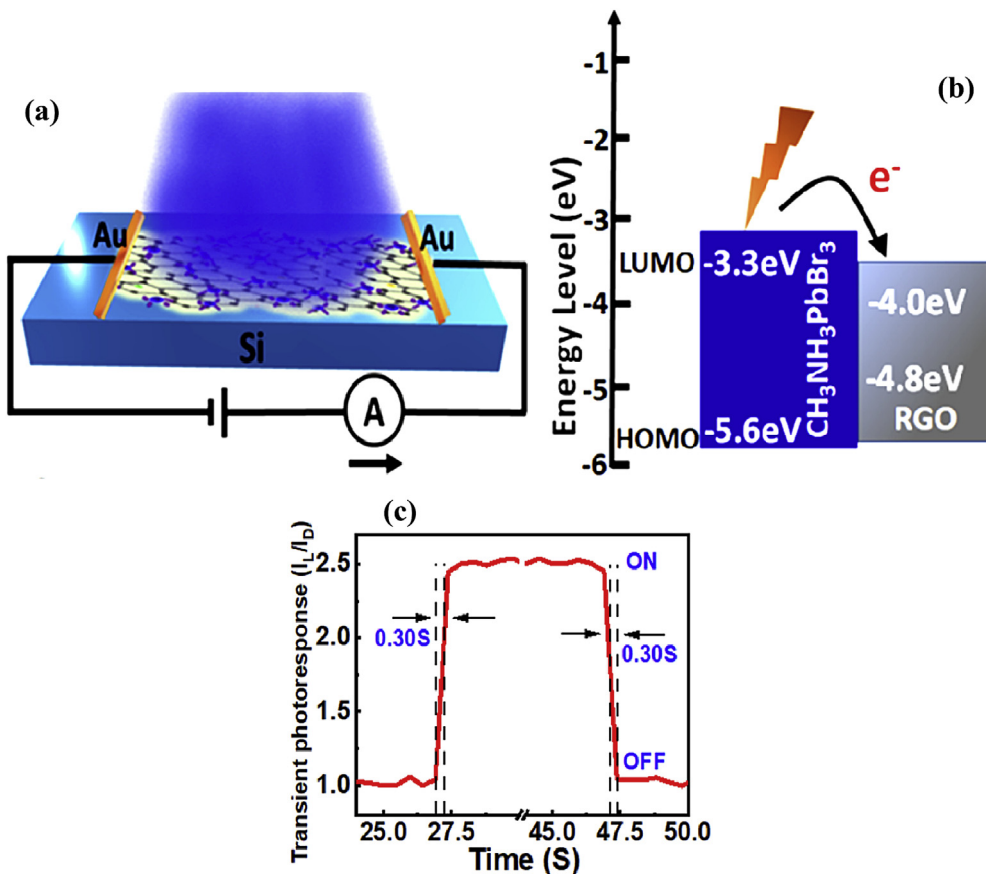


Fig. 6. (a) Graphic of the GPQD-RGO photodetector, (b) energy band diagram of GPQD-RGO sample, and (c) transient photoresponse of ON and OFF conditions for one cycle under light illumination of 442 nm (Chowdhury et al., 2020).

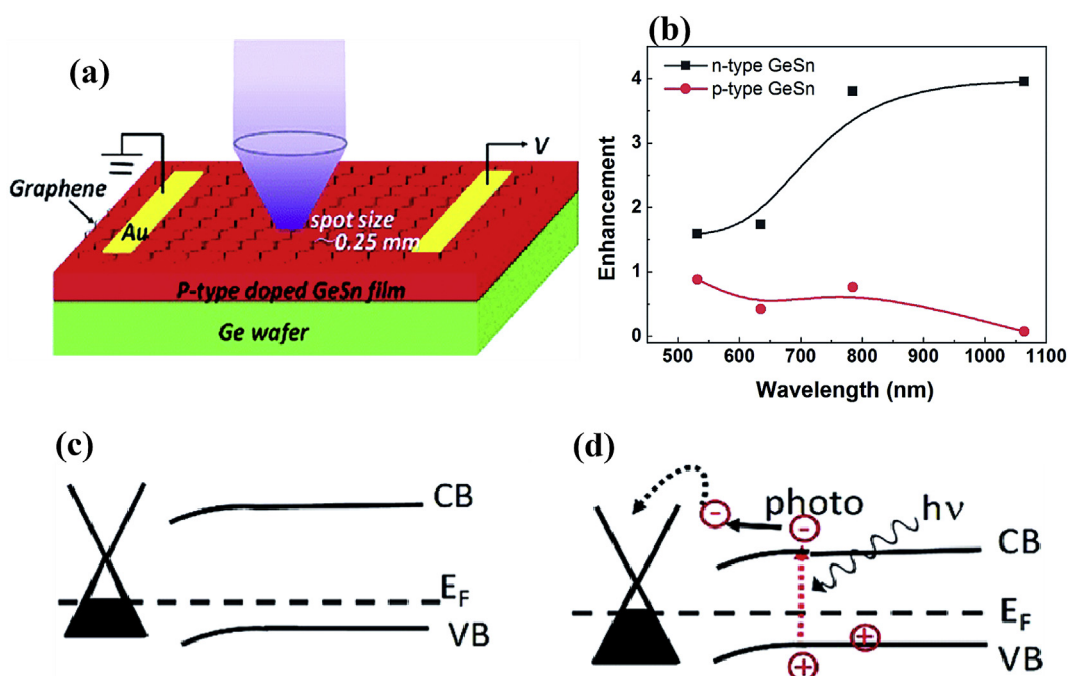


Fig. 7. (a) Schematic grapheme/p-type doped-GeSn device, (b) enhancement factor of photocurrent for grapheme/n-GeSn and grapheme/p-GeSn as a function of excitation wavelength; energy band diagram during (c) without laser and (d) with laser illumination on grapheme/p-type doped-GeSn device (Lv et al., 2020).

the constructive interface-induce effect between WSe₂ and rGO in the rGO/WSe₂. In addition, rGO/WSe₂ photodetectors provided an intense spectral response in the UV-visible region (300–700 nm) than in longer wavelengths.

Very recently, graphene/doped GeSn vertical heterostructures reported for its favorable visible photodetector performance (Lv et al., 2020). Specifically, they developed the monolayer graphene on doped GeSn. Fig. 7(a) presents the basic structural design of graphene/doped GeSn photodetector. It was found that photo-generated charge carriers significantly separated and transferred after addition of graphene monolayer. The enhancement in the photocurrents under various wavelength regions is shown in Fig. 7(b). It should be noted that the enhancement was relatively increased with the laser wavelength in n-type GeSn photodetector compared to the p-type GeSn. Accordingly, Fig. 7(c) depicts the band alignment between graphene and p-type GeSn in the graphene/p-type GeSn heterostructure. Especially, under laser illumination, charge transportation occurred from p-type GeSn to graphene (Fig. 7(d)). Under such constructive heterojunction formation, the visible light responsivity was found to be 200 mA/W. It is to be noted that the presence of graphene monolayer of graphene/doped GeSn composite can be not only acted as an electron transport layer but also provided a broadband photodetection from 532 to 1832 nm.

3.2. Nanostructured based visible photodetectors

Another transition metal dichalcogenides of MoS₂ also contributed its importance towards visible light photodetector performance. In such a way, MoS₂ combined with CdSe (CdSe/MoS₂). Here, CdSe nanoplates vertically assembled on monolayer

MoS₂ using two-step CVD method (Yuan et al., 2019). In this study, the CdSe/MoS₂ photodetector was developed on the SiO₂/Si substrate. Moreover, the photodetector activity studied under the development and patterning of Ti/Au metals using electron beam evaporation and electron beam lithography, respectively. Under constructive interface between CdSe and MoS₂ in the CdSe/MoS₂ heterostructure, ultra-fast photoresponse time of ~370 μs and high photoresponsivity of 12 A/W were achieved under visible light illumination (upon 637 nm). Thus, CdSe/MoS₂ composite was prevailed another interesting feature such as efficient charge carrier transportation. On the basis of above features, CdSe/MoS₂ can act as an emerging visible light photodetector.

Combining of different sulfide materials is also a challenging task for studying the visible light photodetector performance. Thus, SnS/CdS heterojunction photodetector was successfully fabricated, which works under the strategic pyroelectric and photoelectric effects (Chang et al., 2020). During the fabrication of SnS/CdS heterostructure, CdS nanorod arrays synthesized using hydrothermal process on the FTO substrate. Later, SnS nanoflakes were coated on CdS. Finally, Au electrodes were deposited on SnS/CdS using thermal evaporation technique. Fig. 8(a) presents the schematic representation of heterostructured SnS/CdS photodetector developed on FTO substrate. From the photoresponse perspective, SnS/CdS nanostructure potentially studied as a function of time under different visible light wavelengths (365 nm, 405 nm, 532 nm, and 650 nm). From the Fig. 8(b), sharp spikes were observed under both switching light on and off states, which was mainly due to the pyroelectric effect. It is interesting to note that different pyroelectric-photoelectric effects observed in four stages. Fig. 8(c) illustrates the different mechanisms during the photodetector performance. Under visible light, temperature gradient was

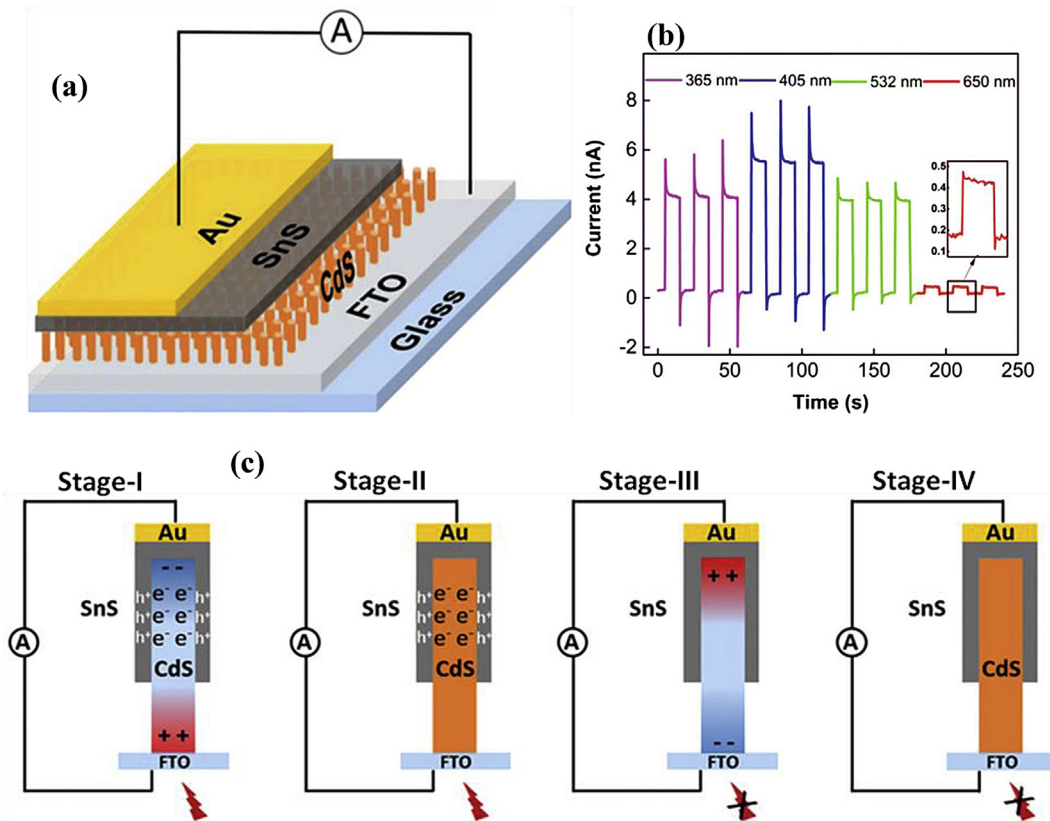


Fig. 8. Schematic (a) structural diagram of SnS/CdS heterojunction photodetector, (b) photoresponse as a function of time under different visible light illuminations, and (c) fundamental working mechanism on the coupled pyroelectric-photoelectric effects (Chang et al., 2020).

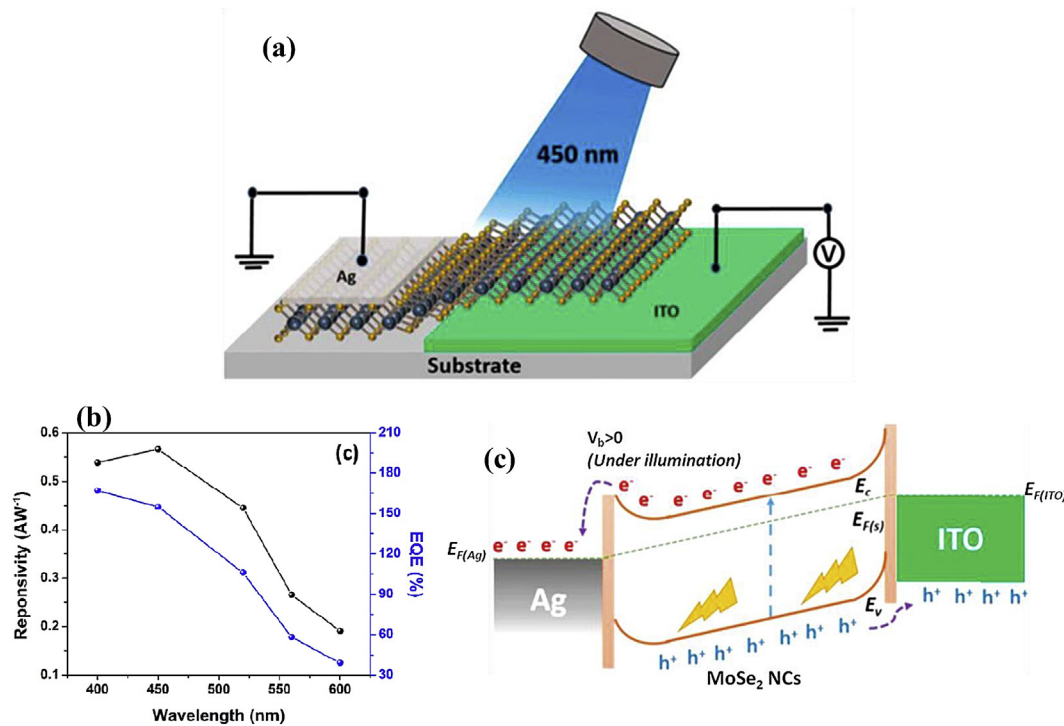


Fig. 9. (a) 3-D graphic drawing of Ag/MoSe₂ NCs/ITO photodetector, (b) responsivity and EQE plots of Ag/MoSe₂ NCs/ITO photodetector at different incident wavelengths, and (c) carrier transport mechanism of the photodetector under $V_b > 0$ illumination condition (Patel et al., 2020).

established across the device as presented in stage-I. This temperature gradient leads to the pyroelectric current at first and then disappeared when temperature gradient becomes zero. Thereafter, photoelectric current prevails under light illumination in stage-II. In the light off stage, the current goes to negative value and comes back to zero in stage-III and IV. It should be highlighted that extra pyroelectric current was mainly due to the internal pyroelectricity of CdS nanorods. Accordingly, SnS/CdS nanostructure device exhibited superior visible photodetector performance at low temperatures. Specifically, under visible light (650 nm and 0.08 mW/cm²), the SnS/CdS nanostructure achieved the responsivity (10.4 mA/W), detectivity (3.56×10^{11} Jones), and response time (less than 30 ms) at 130 K. Overall, the SnS/CdS nanostructure strengthened visible light absorption under pyroelectric and photoelectric efficiency of nanostructured SnS nanoflakes and CdS nanorods.

Understanding of photodetector performance by developing the low-dimensional nanostructures is also necessary compared to the conventional thin films, which manifest the superior photodetector performance. In such a way, single-crystalline MoSe₂ nanocrystals (NCs) were synthesized via liquid exfoliation method for achieving the visible light photodetector performance (Patel et al., 2020). Here, the MoSe₂ layer developed on the ITO substrate using electrophoresis deposition (EPD) technique and Ag was used as electrode material as shown in Fig. 9(a). Such a device fabrication led to the superior responsivity (566 mA/W) and EQE (155%) (Fig. 9(b)). Also, specific detectivity of 3.69×10^{11} Jones was achieved. These results suggest the formation of ohmic-contact at the interface of Ag and MoSe₂, which leads to the high electron density at the surface states. Moreover, absorption and desorption of oxygen molecules facilitated many trap levels, which occupied by the photogenerated charge carriers and avoided recombination rate. Fig. 9(c) illustrates the charge carrier transport mechanism of MoSe₂ NCs photodetector under visible light (450 nm) at bias

voltage > 0 V.

In addition to the above nanorod, nanoflakes and nanocrystal based visible light photodetectors, ultra-long catalyst-free WO₃ nanowires (WO₃ NWs) were synthesized using CVD technique towards high-performance visible photodetector (Wang et al., 2020b). In this system, WO₃ NW was deposited on the SiO₂/Si substrate. The electrode pattern was designed by standard photolithography method. Finally, Cu/Au electrodes were deposited using thermal evaporation technique. Accordingly, superior visible light photodetector performance (responsivity of 19 A/W and detectivity of 1.06×10^{11} Jones) was achieved under 404 nm laser light of intensity 71.23 mW/cm² at a bias voltage of 0.1 V. The superior photodetector performance is attributed to the formation of defect less nanowires, high crystallinity, and high surface-to-volume ratio (Zhu et al., 2016; Wen et al., 2016; Li et al., 2015; Cheng et al., 2017).

In conclusion, favorable formation of graphene-based materials (doped and heterostructure based) and various nanostructured materials are crucial for achieving the superior visible light photodetector performance. Among these, graphene-based heterostructure (GaN/SLG) achieved superior responsivity (400 A/W) and detectivity (208×10^{12} Jones) compared to the CdSe/MoS₂ nanocomposite (responsivity of 10.04 mA/W and detectivity of 3.56×10^{11} Jones). A prominent feature for attaining a high performance is ultra-high mobility of graphene. On the other hand, nanostructure orientation of MoSe₂ single crystal and WO₃ nanowires also considered for achieving superior photodetector performance under visible light. Among all the above photodetectors, WO₃ NWs demonstrated commendable responsivity (19 A/W) and detectivity (1.06×10^{11} Jones). In a word, noteworthy feature of WO₃ in nanowire structure provides potential feature as a graphene-free visible photodetector. Finally, photodetector performance of various visible light photodetectors based on nanostructure formation and graphene source compared in Table 2.

Table 2

Recent results on visible photodetector performance with different materials.

Material	Methodology	Photocurrent (μA)	Responsivity (A/W)	Detectivity (Jones)	EQE (%)	Ref
rGO–CZS	Hydrothermal	—	18.5×10^{-3}	2.08×10^{12}	—	Mathew et al. (2020)
PQD-RGO	Drop casting	—	1.07×10^3	1×10^{13}	—	Chowdhury et al. (2020)
GaN/N-SLG	CVD	16.5×10^3	400	2.89×10^{12}	—	Sankaranarayanan et al. (2020)
GO-PbI ₂	Microwave	—	0.182	1.79×10^{11}	42	Sharma et al. (2020)
RGO/1T-WSe ₂	Step Hydrothermal	90	105	—	—	He et al. (2020)
Graphene/GeSn	MBE	—	0.2	—	—	Lv et al. (2020)
CdSe/MoS ₂	CVD	10×10^{-3}	12	—	—	Yuan et al. (2019)
SnS/Cds	Hydrothermal	7.12	10.4×10^{-3}	3.56×10^{11}	—	Chang et al. (2020)
MoSe ₂ NCs	Liquid exfoliation	—	566×10^{-3}	3.69×10^{11}	155	Patel et al. (2020)
WO ₃	CVD	—	19	1.06×10^{11}	—	Wang et al., (2020b)

4. Research progress on IR based photodetectors

Unlike the UV and visible light photodetector, infrared (IR) photodetectors are mainly employed in astronomy and defence areas. In this situation, higher wavelengths are required to detect the objects and targets. Defence applications include distinguishing decoys from actual missiles, locating landmines during aircraft landing, and identification of warm targets against a warm background. The current video camera industry has been dominated by the basic charge coupled device (CCD) detector technology. However, the latest technological advancements in mass production of IR detectors led to include it in video camera applications as well. Therefore, it is necessary to develop the low-cost IR PDs with high-end device parameters such as sensitivity, spectral selectivity, working temperature, and peak wavelength (Zeng et al., 2013; Chakrabarti et al., 2004; Tezcan et al., 2003). Currently, HgCdTe-based IR photodetectors have been using in astronomical applications, which possess superior responsivity and ultra-low noise detection in the long-wave infrared regime (LWIR) (Elliott, 1998). But, high cost, non-uniformity over a large area, and lack of availability of substrates are the limitations associated with the HgCdTe-based IR detectors (Rogalski, 2005). To overcome, InAs-(In–Ga)Sb based IR photodetectors were developed as alternative to the HgCdTe-based detectors, which showed promising features due to their low dark-currents and high quantum efficiency (Claro et al., 2020; Wu et al., 2016b; Pan et al., 1998). Moreover, employing Si and InSb based materials are predicted to outperform the very long-wave infrared regime (VLWIR) and mid-wave infrared regime (MWIR) performance (Tran et al., 2019; Xie et al., 2015). Surprisingly, IR detector technologies operate specifically at cryogenic temperatures and variation in the temperature would alter the detection range of the device. For burgeoning the infrared detector technology, quantum well-infrared photodetectors (QWIPs) used for MWIR detection, which commercially well established in the current market (Levine et al., 1992; Gunapala et al., 1991; W. Tang et al., 2018; Rodriguez et al., 2018; Wu et al., 2018). It is interesting to highlight that quantum dot infrared photodetectors (QDIPs) used for LWIR and VLWIR detection (Ramiro et al., 2020; Chen et al., 2020c). Specifically, QDIPs are commendable to overcome the QWIPs technology towards MWIR detection. Currently, various research groups involved in developing the promising quantum dot technology for strengthening the optical properties due to the fact that electrons are confined in 3-D space (Keuleyan et al., 2011). Remarkably, QDIPs possess superior properties compared to QWIPs such as outstanding charge carrier lifetime (10–100 times), grating free usage, and more stable during temperature fluctuations. In this section, we mainly focused on the

various QDIPs based on its charge transportation mechanism for achieving superior IR light detection.

4.1. InAs-based quantum dot infrared photodetectors

In a bid to develop the IR photodetector, self-assembled 50 layers of InAs QDs with 30 nm thickness of GaAs spacers separating them was developed on the <100> GaAs substrate (InAs/GaAs QDIPs). Then, InAs/GaAs QDIPs were sandwiched between the collector and emitter (Liu et al., 2001). By this method, InAs/GaAs QDIPs attained responsivity about 0.1 A/W at an IR wavelength of 5000 nm (80 K). Ideally, superior response range was provided by the QDIPs under reduced density of states. In doing so, QDIPs responsible for the variety of possible transitions, it become crucial for the occupancy of QD states.

Based on emerging IR photodetector of QDIPs, another composite based on GaAs QDIPs (InAs/InGaAs/GaAs QDIPs) was developed by molecular beam epitaxy (Kim et al., 2004). In this work, different monolayer (ML) QDs such as InAs(2-ML), In_{0.15}Ga_{0.85}As(20-ML) and GaAs(130-ML) have been utilized to develop the InAs(2-ML)/In_{0.15}Ga_{0.85}As(20-ML)/GaAs(130-ML) heterostructure. The resultant composite sandwiched between highly Si-doped GaAs as top and bottom contacts. Notably, the InAs/InGaAs/GaAs QDIPs framework exhibited superior detectivity about 33×10^{11} Jones at 9.3 μm IR wavelength. Also, extreme low noise (10^{14} A/Hz^{1/2}) was observed at 1.4 V and 78 K, which were higher than the previously reported QDIPs (mention the value) (Ye et al., 2002). In conclusion, the optimized heterostructure of InAs/InGaAs/GaAs QDIPs have exhibited high responsivity of 700 mA/W, it was mainly attributed to the enlarged IR absorption under increased QD layers.

Similarly, Al_{0.3}Ga_{0.7}As/GaAs heterostructure including InAs quantum-dot (QD) layer with a 10 nm thick GaAs spacer was developed as a mid-infrared sensor (Murata et al., 2020). The photodetector developed on n⁺-GaAs (001) substrate using molecular beam epitaxy (MBE) technique. Later, intrinsic GaAs layer (300 nm), InAs QDs, GaAs capping layer (10 nm), and Al_{0.3}Ga_{0.7}As layer (20 nm) were sequentially developed. Au and Au–Ge electrodes were used to achieve the ohmic-contact behaviour between the electrode and photo-active material. As a result, Al_{0.3}Ga_{0.7}As/GaAs composite exhibited the responsivity of 0.8 A/W at 295 K and specific detectivity of 1.8×10^{10} Jones under 6.6 μm IR wavelength illumination. The accumulated electrons at the interface of heterostructure transferred to the conduction band of Al_{0.3}Ga_{0.7}As barrier by means of two factors. The first one can be illumination of IR light and other factor was drift produced by the electric field at the junction. Fig. 10(a) presents the energy states for limited charge

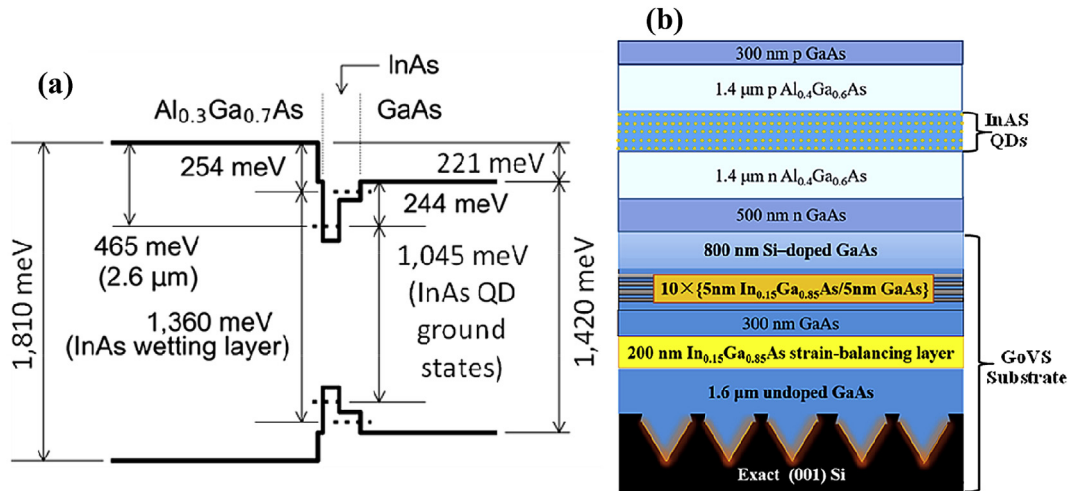


Fig. 10. (a) The proposed energy states for limited carriers at the hetero-interface of TPU-SC with InAs QDs (Asahi et al., 2017) and (b) Graphic illustration of InAs QD avalanche photodiodes deposited on GoVS substrate (Chen et al., 2020a).

carriers at the hetero-interface of two-step photon up-conversion-solar cell (TPU-SC) with InAs QDs (Asahi et al., 2017). The presence of InAs QDs significantly induces the intraband transitions, which was mainly due to the electronic wave functions spatially quantized by the QDs irrespective of the incident light polarization (Tas et al., 2012).

Very recently, avalanche photodiode (APD) based InAs quantum dot IR photodetectors were studied under low dark current generation (Chen et al., 2020b). The QD-APD was deposited on GaAs-on-V-grooved-Si (GoVS) substrate by metal-organic chemical

vapor deposition technique (MOCVD). APD epitaxial structure was developed using molecular beam epitaxy (MBE). After deposition, the epitaxial structure was etched into a wave guide shape by inductive coupled plasma. Then the sidewalls of wave guide were passivated with Al₂O₃ layer to arrest the leakage current. In such a way, Pd/Ti/Pd/Au and Pd/Ge/Pd/Au were used as metal stack contacts. Fig. 10(b) presents the overall layer-by-layer device architecture of InAs QD avalanche photodiodes deposited on GoVS substrate. Here, InAs quantum dot waveguide APD was monolithically deposited onto the Si substrate. Accordingly, the

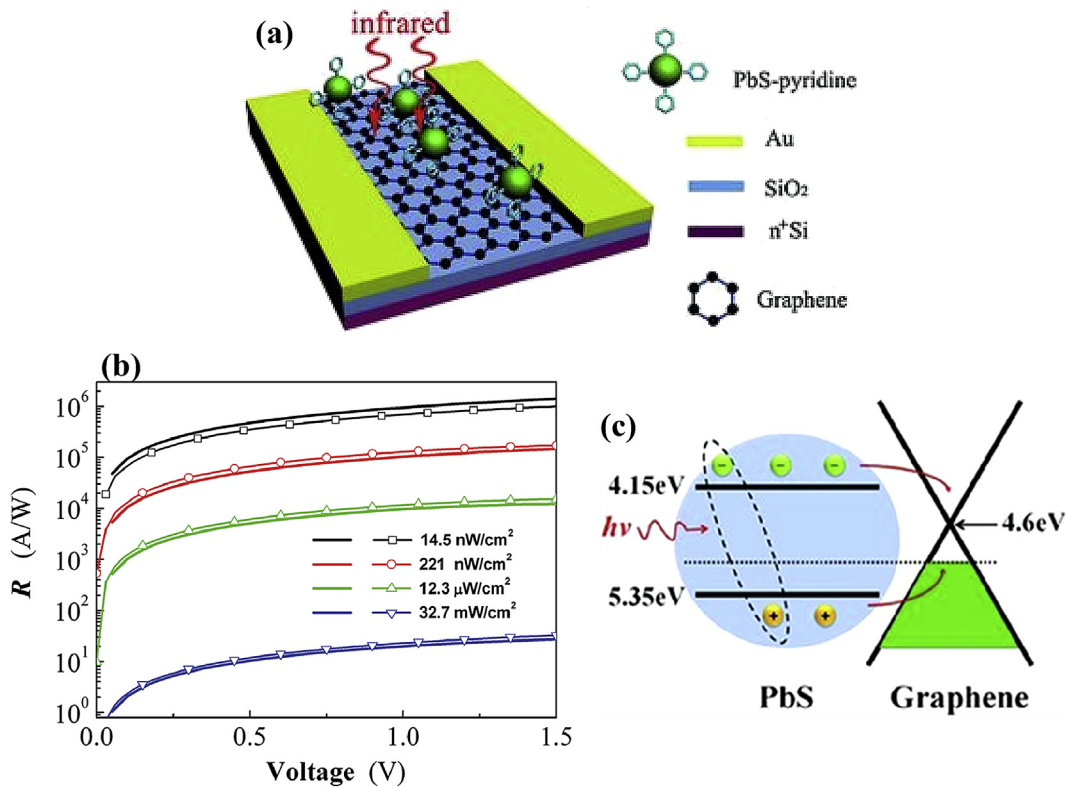


Fig. 11. (a) Graphic diagram of graphene transistor tailored with PbS QDs, (b) responsivity of PbS QD/graphene heterojunction under the IR illumination with different IR intensities, and (c) band diagram along with charge generation at a PbS QD/graphene heterojunction under the IR illumination (Sun et al., 2012).

fabricated device exhibited the lower dark current (0.1 nA) with responsivity of 0.234 A/W.

4.2. Pb, Ge and Hg based quantum dot infrared photodetectors

In addition to the above InAs QDs community, PbS QDs also streamlined to achieve superior IR photodetection. Building upon this knowledge on PbS QDs, graphene integrated PbS QDs identified as efficient IR photodetector (Sun et al., 2012). To prove viability of PbS QDs, graphene sheets were synthesized on the copper substrate by conventional CVD technique. Later, graphene sheets were transferred onto the Si substrate. Finally, PbS QDs developed onto the graphene using facile solution processing technique. Fig. 11 (a) presents the graphene modified PbS QDIP device structure. In this creative study, IR responsivity of PbS QDs based device significantly increased with decrease of light intensity ($32.7 \text{ mW/cm}^2 < 12.3 \mu\text{W/cm}^2 < 221 \text{ nW/cm}^2 < 14.5 \text{ nW/cm}^2$). They found that PbS QDIP device is capable of superior responsivity of $1 \times 10^7 \text{ A/W}$ at a selective low IR light (895 nm) intensity of 14.5 nW/cm^2 as shown in Fig. 11 (b). On the other hand, the PbS QDIP device was also developed on the flexible plastic substrate, which provided excellent channel for the development of flexible photodetector. Considering the interaction between PbS-QDs and graphene sheets, it is plausible to expect the high detection capability, which remains an attractive feature for superior charge transportation from PbS-QDs to graphene (with high mobility). The corresponding energy levels alignment between graphene and PbS-QD, charge carrier generation and separation under IR illumination presented in the Fig. 11(c).

In another study, high-speed PbSe QD photodetector was fabricated using sandwich micro-strip transmission line structure (Gao et al., 2016). Here, solution processed PbSe-QD films sandwiched between ITO electrode (bottom) and gold electrode (top). This device architecture was particularly noticeable for ultra-high-speed IR photodetector performance with EQE of ~50%, responsivity of 0.36 A/W , and response time of 74 ps at room temperature under carrier sweep mechanism. Such a striking IR photodetector performance realized by the tiny overlapping area of $100 \mu\text{m}^2$ electrodes.

Although limited research focused on spectral selective photodetection, the unique structure of PdS QDs ground for the spectral selective IR photodetector performance (ss-Pds) (Qiao et al., 2016). In this work, they reported the absorption characteristics (at wavelengths of 800 nm, 880 nm, 1140 nm, and 1480 nm) powered by the QD size effect. The organolead triiodide perovskite (OTP) was

used as top layer to absorb the UV and visible spectra. The detection range was able to tune from 800 nm to the onset absorption wavelength of the bottom-QD layer through the OTP/QD ss-PDs. Further, depending on the size of the QDs, we can achieve the essential IR detection range. Based on the above constructive features, QD ss-PDs achieved superior responsivity (15.6 mA/W) and detectivity ($1.3 \times 10^{11} \text{ Jones}$) under IR light (930 nm). Therefore, introduction of OTP as a top layer can highly beneficial for removal of non-target spectrum, which is energetically favorable for selective IR detection.

Another type of PbS QD based composite favorable for the IR photodetector performance. Interestingly, graphene-PbS QD composite provided unique opportunity to study the near-infrared photodetector performance (Jeong et al., 2020). Initially, single-layer graphene flakes and PbS QDs capped with oleic acid were separately synthesized. Later, the solution was mixed using conventional sonication process in hexane solution. Finally, the graphene-PbS QDs mixture was coated onto a glass substrate. The interdigitated finger patterns of Au electrodes were patterned onto the SiO_2 substrate using the photolithography. Due to the constructive interaction between graphene and PbS QDs, graphene-PbS QDs composite exhibited higher photocurrent (5 times), 22% of less rise time and 47% of shorter decay time compared to the pure PbS QDs. Overall, the impressive enhancement in the photodetector performance mainly ascribed to the photo-induced charge transportation in the graphene-PbS QD composite.

Recently, the concept of large-scale production of spray deposited PbS QDs addressed for IR photodetector (Chen et al., 2020c). This approach also compared with the QD-solids prepared by the simple spin-coating technique. The spray deposition technique allows the QDs to establish the dense packing. Fig. 12(a) presents the PbS QDs photodetector device structure. Due to the dense packing, charge carrier density can be improved, and band gap can be narrowed among the neighboring QDs. Taking into the account, IR photodetector performance can be significantly increased. Fig. 12(b) presents the IR photodetector performance of spray and spin coated PbS QDs. The spray deposited samples determine the higher photon currents compared to the spin coated PbS QDs over range IR wavelengths (800–1400 nm) with intensity of $430 \mu\text{W/cm}^2$. As a result, spray deposited PbS QDIPs exhibited superior responsivity (365.1 A/W) and detectivity ($1.4 \times 10^{12} \text{ Jones}$) under IR light of wavelength 1250 nm with intensity of $63.5 \mu\text{W/cm}^2$. Finally, this study considers the importance of spray deposition technique for developing the potential large-scale IR photodetectors.

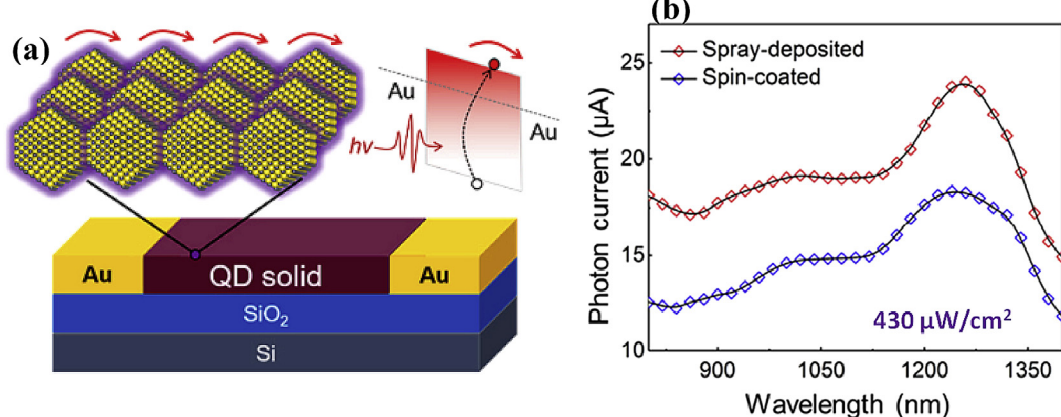


Fig. 12. (a) PbS quantum dots photodetector device and (b) photon current behavior of spin and spray coated PbS quantum dots photodetector (Chen et al., 2020c).

Table 3

Comparison of IR photodetector performance with different nanostructured materials.

Materials	Methodology	Photocurrent (μA)	Responsivity (A/W)	Detectivity (Jones)	EQE (%)	Ref
InAs QDs	MBE	—	0.7	33×10^{11}	—	Kim et al. (2004)
$\text{Al}_{0.3}\text{Ga}_{0.7}\text{As}/\text{GaAs}/\text{InAs}$ QDs	MBE	20	0.8	1.8×10^{10}	—	Murata et al. (2020)
InAs QD APD	MOCVD	—	0.234	—	—	Chen et al. (2020a)
PbS-QDs/graphene	CVD	6×10^3	1×10^7	—	—	Sun et al. (2012)
PbSe QDs	Dip coating	—	0.36	—	50	Gao et al. (2016)
Ss PbS QDs	Spin coating	—	15.6×10^{-3}	1.3×10^{11}	—	Qiao et al. (2016)
Graphene-PbS QD	Sonication	5.4×10^{-3}	—	—	—	Jeong et al. (2020)
PbS QD	Spray deposition	—	365.1	1.4×10^{12}	—	(Chen et al., 2020c)
SWCNT-PbS QD	Spin coating	31.1	7.2	7.1×10^{10}	—	Tang et al. (2018)
GeQD/SiNW	PECVD	22×10^{-3}	1.5×10^{-3}	—	—	Zhao et al. (2020)
HgSe/HgTe NC	Spin coating	10×10^{-3}	$\sim 1 \times 10^{-3}$	1.5×10^9	—	Livache et al. (2019)
GNR	Drop casting	2725	1	—	—	Chitara et al. (2011)

Further, adaptive single-walled carbon nanotubes (SWCNTs) combined with PbS QDs (SWCNT-PbSQD), which directed to achieve IR photodetector performance (Y. Tang et al., 2018). For SWCNT-PbSQD, SWCNTs were deposited on the Si/SiO₂ substrate using the dip-coating method. The interdigitated electrode pattern was designed using electron beam lithography. Later, this pattern allows to develop the Pd (3 nm) and Au (50 nm) electrodes using thermal evaporation technique. Finally, PbS QD solution was adapted as layer by layer using spin coating on SWCNTs. As a result, the developed SWCNT-PbSQD architecture underlined the responsivity of 7.2 A/W, specific detectivity of 7.1×10^{10} Jones, and response time of 1.58 ms at IR wavelength of 1550 nm (141.47 mW/cm²). At the most fundamental level, internal electric field approximated the light-induced charge carrier separation at the interface of SWCNT and PbSQDs. Overall, SWCNT-PbSQD combination is essential for superior IR photoresponse and detectivity.

In a similar vein, germanium quantum dot (GeQDs) infrared photodetectors were developed at low temperature (<300 °C) (Zhao et al., 2020). In this method, the Si–Ge bilayer was converted into Si/Ge heterostructured nanowires by rolling of indium (In) droplets at 300 °C. Later, Indium droplets absorbed into the bilayer precursor and self-modulated to produce GeQDs. Interestingly, SiNWs as a metal electrode demonstrated the possibility of superior IR absorption. As a result, the developed samples have shown the IR responsivity about 1.5 mA/W (at $\lambda = 1550$ nm). It demonstrates the possibility to integrate the individual GeQDs into Si complementary metal oxide semiconductor (CMOS) circuits towards IR detection, high-density IR communication, and imaging.

Colloidal nanocrystals also extensively used, since they have the ability to achieve the broad spectral tunability (Livache et al., 2019). reported that energy landscape of quantum well and quantum dot IR photodetectors aped from combination of mercury selenide (HgSe) and mercury telluride (HgTe) nanocrystals. This strategic metamaterial combination provides intraband absorption under superior transport properties such as fast time response, low dark current, and large thermal activation energy. In such a way, the responsivity and detectivity values were found to be ~5 mA/W and 1.5×10^9 Jones, respectively at 80 K. The obtained results were very less compared to the QDIPs (Deng et al., 2014). The reason behind the less responsivity is lack of absorption through the very thin layer of NCs.

While the usage of ultrahigh mobility graphene exhibits promising visible light photodetector performance, it is limited in the IR region about 2% and resulting low responsivities. To study the capability of IR photodetector performance, rGO combined graphene nanoribbons (GNR) were developed on SiO₂/Si substrate using drop casting method (Chitara et al., 2011). Here, two electrodes (Cr/Au) were coated in between rGO/GNR, which can give rise to the IR responsivity of 1 A/W. Thus, there are many challenges

to improve the IR photodetector performance of graphene, which can be solved by developing multilayer stacking on Si substrate. As a result, multilayer stacking can scale up the IR absorption capacity up to ~25%, which is comparatively higher than bi-layer (4.6%) and tri-layer (6.9%) of graphene under normal incident of IR light at 1550 nm wavelength.

In conclusion, we have systematically discussed the viability of InAs and PbS based QDs towards efficient IR photodetector performance. In an attempt to address the IR photodetector performance based on InAs QDs, $\text{Al}_{0.3}\text{Ga}_{0.7}\text{As}/\text{GaAs}$ hetero-structure consisting of InAs QDs exhibited outstanding IR responsivity (0.8 A/W) at 6.6 μm wavelength compared to the other InAs QD photodetectors. Moreover, QDIPs based PbS QDs have shown improved IR photodetector performance compared to the InAs-based photodetectors. In such a way, PbS-QDs/graphene composite achieved remarkable responsivity (10^7 A/W) under IR irradiation, which attributed to the superior charge carrier transportation at the interface under ultrahigh mobility of graphene. Also, the possibility of deposition technique (spray deposition) makes the PbS QDs more responsive to encourage the IR light (365 A/W) and detectivity (1.4×10^{12} Jones) under controlled higher density of PbS QDs. On the other hand, HgSe/HgTe nanostructures presented poor responsivity due to absorption layer of HgSe/HgTe nanocrystals was very thin. The mechanism of generating photocurrent in QDIPs is due to intraband excitation of electrons upon illumination with photons. The photo-excitation of electrons takes place from confined states of conduction band dots to the continuum. Improved QDIPs performance could be due to lower dark current attributed to the 3-D confinement of electron wave function, reduction in thermal generation of electrons due to quantization of energy in all three dimensions, and ability to inter-sub-band absorption even at normal incidence. The comprehensive IR photo-detection performance of various QDs is tabulated in Table 3.

5. Conclusions and future perspectives

In this review, we have systematically summarized the recent advancements in UV, visible, and IR photodetectors based on various adaptive heterostructures. Specifically, we categorized the novel functional materials such as (i) metal oxide thin films for UV light detection, (ii) 1-D nanomaterials (NWs), 2-D nanosheets and perovskite materials for visible light detection and (iii) 0-D (QDs, NCs) for IR detection. Also, we emphasized the various device architectures, which significantly influenced the overall photodetector performance.

In depth, metal-oxide semiconductors (ZnO, Ga₂O₃, SnO₂, TiO₂, and WO₃) were given priority for UV light detection owing to their suitable wide bandgap. For visible light photodetectors, we have systematically explored the graphene-based materials with

different heterostructures (PQD/rGO, GaN/SLG, rGO/WSe₂ and GeSn/graphene) and nanostructures (HgSe/HgTe NCs and WO₃ NWs) owing to their broad band spectral absorption and ultra-high mobility of graphene. However, due to the low absorption rate of pure graphene, graphene-based composites (rGO-CZS, PQD-rGO, N-SLG, and GO doped PbI₂) dedicated to improve the photo-response and EQE of resultant photodetector. It is to be noted that photogenerated charge carriers effectively separated at the heterostructure interface to enhance the responsivity and detectivity. Further, by synthesizing the nanostructures with high surface-to-volume ratio, the bandgap values were effectively tuned (WSe₂ and WO₃), which was highly beneficial for visible light absorption and good responsivity. For IR photodetectors, mostly QD-based materials (InAs QDs and PbS QDs) have been successfully utilized. Among all QDs, QDIPs showed excellent photoresponse in LWIR and MWIR owing to its 0-D quantum confinement and ability to absorb the light with any polarization.

Although immense research is being conducted on photodetector performance in various light regions, researchers further facing many challenges in extruding the superior photosensitivity. Some of the future challenges and perspectives are presented below.

- 1) There is plenty of room for further improvement in the responsivity and detectivity of the next-generation flexible photodetectors.
- 2) Also, we needed to convert them into self-powered PDs under strategic experimental methods.
- 3) Control over the crystal growth, orientation, thickness, morphology, uniformity, and repeatability of the photodetector is necessary.
- 4) Scaling up of large-scale production and cost reduction required for our future generations. As discussed in the present review paper, several chemical methods have been adopted to synthesize different nanostructures, which succeeded band gap tuning. Nanostructured PDs exhibited higher photoresponse compared to the thin film PDs. However, they exhibited the ultra-fast response to the incident radiation.
- 5) The higher response time of nanostructure PDs limits their applicability in the development of ultrafast optoelectronic devices. On the other side, thin films and heterostructured devices show fast response to the incident photons. Further, nano heterostructures were exhibited high responsivity and low response time. Hence, nano heterostructures based PDs should be given more attention to address the current requirements in ultrafast optoelectronic devices.
- 6) Also, various physical fabrication methods to be employed to achieve longer lifecycles and scalability in photodetector field.

Finally, we elaborately reviewed and correlated the recent progress on UV, visible, and IR photodetectors performance of various nanostructures. In conclusion, this review could lead the research for developing the multi-spectral photodetectors by integrating different nanostructures and adopting appropriate device configurations.

Credit author statement

P.V. Karthik Yadav: Writing – original draft, Data curation, B. Ajitha: Data curation, Visualization, Writing – original draft, Y. Ashok Kumar Reddy: Conceptualization, Visualization, Writing – review & editing, Supervision, Adem Sreedhar: Visualization, Validation, Writing – review & editing.

Declaration of competing interest

The authors declare that they have no known competing financial interests or personal relationships that could have appeared to influence the work reported in this paper.

Acknowledgements

One of the author (Dr. Y. Ashok Kumar Reddy) would like to express his gratitude to the Department of Science and Technology (DST), New Delhi, India for the award of DST-Inspire Faculty (DST/INSPIRE//04/2017/002531).

References

- Ahmadi, M., Wu, T., Hu, B., 2017. A Review on Organic-inorganic halide perovskite photodetectors: device engineering and fundamental physics. *Adv. Mater.* 29, 1605242.
- Ali, G.M., Chakrabarti, P., 2012. Fabrication and characterization of thin film ZnO Schottky contacts based UV photodetectors: a comparative study. *J. Vac. Sci. Technol. B* 30, 031.
- Ali, G.M., Moore, J.C., Kadhim, A.K., Thompson, C., 2014. Electrical and optical effects of pd microplates embedded in ZnO thin film based MSM UV photodetectors: a comparative study. *Sensors Actuators, A Phys.* 209, 16–23.
- Ates, E.S., Kucukyildiz, S., Unalan, H.E., 2012. Zinc oxide nanowire photodetectors with single-walled carbon nanotube thin-film electrodes. *ACS Appl. Mater. Interfaces* 4, 5142–5146.
- Asahi, S., Teranishi, H., Kusaki, K., Kaizu, T., Kita, T., 2017. Two-step photon up-conversion solar cells. *Nat. Commun.* 8, 14962.
- Balandin, A.A., 2011. Thermal properties of graphene and nanostructured carbon materials. *Nat. Mater.* 10, 569–581.
- Bera, A., Hajra, P., Shyamal, S., Mandal, H., Sariket, D., Kundu, S., Mandal, S., Bhattacharya, C., 2018. Solvent effects on the photoelectrochemical water oxidation behaviour of TiO₂ semiconductors. *Mater. Today Proc.* 5, 10161–10168.
- Buch, V.R., Chawla, A.K., Rawal, S.K., 2016. Review on electrochromic property for WO₃ thin films using different deposition techniques. *Mater. Today Proc.* 3, 1429–1437.
- Caliskan, D., Butun, B., Ozcan, S., Ozbay, E., 2013. Metal-semiconductor-metal photodetector on as-deposited TiO₂ thin films on sapphire substrate. *J. Vac. Sci. Technol., B* 31, 020606.
- Chakrabarti, S., Roberts, A.D.S., Bhattacharya, P., Gunapala, S., Bandara, S., Rafol, S.B., Kennerly, S.W., 2004. High-temperature operation of InAs-GaAs quantum-dot infrared photodetectors with large responsivity and detectivity. *IEEE Photon. Technol. Lett.* 16, 1361–1363.
- Chang, Y., Wang, J., Wu, F., Tian, W., Zhai, W., 2020. Structural design and pyroelectric property of SnS/CdS heterojunctions contrived for low-temperature visible photodetectors. *Adv. Funct. Mater.* 30, 2001450.
- Chauhan, A.K., Kataria, N., Garg, V.K., 2020. Green fabrication of ZnO nanoparticles using *Eucalyptus* spp. leaves extract and their application in wastewater remediation. *Chemosphere* 247, 125803.
- Cheng, R., Wen, Y., Yin, L., Wang, F., Wang, F., Liu, K., Shifa, T.A., Li, J., Jiang, C., Wang, Z., He, J., 2017. Ultrathin single-crystalline CdTe nanosheets realized via Van der Waals epitaxy. *Adv. Mater.* 29, 1703122.
- Chen, X., Mu, W., Xu, Y., Fu, B., Jia, Z., Ren, F.-F., Gu, S., Zhang, R., Zheng, Y., Tao, X., Ye, J., 2018. Highly narrow-band polarization-sensitive solar-blind photodetectors based on β-Ga₂O₃ single crystals. *ACS Appl. Mater. Interfaces* 11, 7131–7137.
- Chen, X., Ren, F.-F., Ye, J., Gu, S., 2020. Gallium oxide-based solar-blind ultraviolet photodetectors. *Semicond. Sci. Technol.* 35, 023001.
- Chen, B., Wan, Y., Xie, Z., Huang, J., Zhang, N., Shang, C., Norman, J., Li, Q., Tong, Y., Lau, K.M., Gossard, A.C., Bowers, J.E., 2020b. Low dark current high gain InAs quantum dot avalanche photodetectors monolithically grown on Si. *ACS Photonics* 7, 528–533.
- Chen, W., Tang, H., Chen, Y., Heger, J.E., Li, N., Kreuzer, L.P., Xie, Y., Li, D., Anthony, C., Pikramenou, Z., Ng, K.W., Sun, X.W., Wang, K., Buschbaum, P.M., 2020c. Spray-deposited PbS colloidal quantum dot solid for near-infrared photodetectors. *Nanometer Energy* 78, 105254.
- Chetri, P., Dhar, J.C., 2020. Improved photodetector performance of SnO₂ nanowire by optimized air annealing. *2020 Semicond. Sci. Technol.* 35, 045014.
- Chitara, B., Panchakarla, L.S., Krupandhi, S.B., Rao, C.N.R., 2011. Infrared photodetectors based on reduced graphene oxide and graphene nanoribbons. *Adv. Mater.* 23, 5419.
- Cho, H., Joo, H., Kim, H., Kim, J.E., Kang, K.S., Yoon, J., 2021. Improved photoelectrochemical properties of TiO₂ nanotubes doped with Er and effects on hydrogen production from water splitting. *Chemosphere* 267, 129289.
- Chowdhury, F., Pradhan, B., Ding, Y., Towers, A., Gesquiere, A.J., Tetard, L., Thomas, J., 2020. Perovskite quantum dot-reduced graphene oxide superstructure for efficient photodetection. *ACS Appl. Mater. Interfaces* 12, 45165–45173.
- Cook, B., Liu, Q., Butler, J., Smith, K., Shi, K., Ewing, D., Casper, M., Stramel, A.,

- Elliot, A., Wu, J., 2018. Heat-assisted inkjet printing of tungsten oxide for high-performance ultraviolet photodetectors. *ACS Appl. Mater. Interfaces* 10, 873–879.
- Claro, M.S., Stropka, D.G., da Silva, E.C.F., Quivy, A.A., 2020. Strong photovoltaic effect in high-density InAlAs and InAs/InAlAs quantum-dot infrared photodetectors. *Sens. Actuators, A* 315, 112262.
- de Araujo, E.P., Arantes, A.N., Costa, I.M., Chiquito, A.J., 2020. Reliable tin dioxide based nanowire networks as ultraviolet solar radiation sensors. *Sens. Actuators, A A* 302, 111825.
- De Fazio, D., Goykhman, I., Yoon, D., Bruna, M., Eiden, A., Milana, S., Sassi, U., Barbone, M., Dumcenco, D., Marinov, K., Kis, A., Ferrari, A.C., 2016. High responsivity, large-area Graphene/MoS₂ flexible photodetectors. *ACS Nano* 10, 8252–8262.
- Deng, Z., Jeong, K.S., Sionnest, P.G., 2014. Colloidal quantum dots intraband photodetectors. *ACS Nano* 8, 11707–11714.
- Elliott, C.T., 1998. New infrared and other applications of narrow-gap semiconductors. *Proc. SPIE* 3436, 763–775.
- Falkovsky, L.A., 2008. Optical properties of graphene. *J. Phys. Conf. Ser.* 129, 012004.
- Farhati, H., Djeffal, F., Martin, N., 2020. Highly improved responsivity of self-powered UV-visible photodetector based on TiO₂/Ag/TiO₂ multilayer deposited by glad technique: effects of oriented columns and nano-sculptured surface. *Appl. Surf. Sci.* 529, 35–38.
- Flemban, T.H., Haque, M.A., Ajia, I., Alwadi, N., Mitra, S., Wu, T., Roqan, I.S., 2017. A photodetector based on p-Si/n-ZnO nanobud heterojunctions with high ultraviolet responsivity. *ACS Appl. Mater. Interfaces* 9, 37120–37127.
- Fu, Q.M., Peng, J.L., Yao, Z.C., Zhao, H.Y., Ma, Z.B., Tao, H., Tu, Y.F., Tian, Y., Zhou, D., Han, Y.B., 2020. Highly sensitive ultraviolet photodetectors based on ZnO/SnO₂ core-shell nanorod arrays. *Appl. Surf. Sci.* 527, 146923.
- Gao, J., Nguyen, S.C., Bronstein, N.D., Alivisatos, A.P., 2016. Solution-processed, high-speed, and high-quantum-efficiency quantum dot infrared photodetectors. *ACS Photonics* 3, 1217–1222.
- Gunapala, S.D., Levine, B.F., Ritter, D., Hamm, R., Panish, M.B., 1991. InGaAs/InP long wavelength quantum well infrared photodetectors. *Appl. Phys. Lett.* 58, 2024–2026.
- Guo, D., Guo, Q., Chen, Z., Wu, Z., Li, P., Tang, W., 2019. Review of Ga₂O₃-based optoelectronic devices. *Mater. Today Phys.* 11, 100157.
- Hai, Z., Akbari, M.K., Xue, C., Xu, H., Depuydt, S., Zhuiykov, S., 2017a. Photodetector with superior functional capabilities based on monolayer WO₃ developed by atomic layer deposition. *Sens. Actuators, B* 245, 954–962.
- Hai, Z., Akbari, M.K., Xue, C., Xu, H., Hyde, L., Zhuiykov, S., 2017c. Wafer-scaled monolayer WO₃ windows ultra-sensitive, extremely fast and stable UV-A photodetection. *Appl. Surf. Sci.* 405, 169–177.
- He, H.Y., He, Z., Shen, Q., 2020. Excellent photoresponse performances of graphene/metallic WSe₂ nanosheet heterostructure films. *Mater. Sci. Semicond. Process.* 107, 104851.
- He, Z., Liu, Q., Hou, H., Gao, F., Tang, B., Yang, W., 2015. Tailored electrospinning of WO₃ nanobelts as efficient ultraviolet photodetectors with photo-dark current ratios up to 1000. *ACS Appl. Mater. Interfaces* 7, 10878–10885.
- Hitosugi, T., Yamada, N., Nakao, S., Hirose, Y., Hasegawa, T., 2010. Properties of TiO₂-based transparent conducting oxides. *Phys. Status Solidi* 207, 1529–1537.
- Huang, B.R., Saravanan, A., Lu, H.C., 2020. Structural engineering of dispersed graphene flakes into ZnO nanotubes on discontinuous ultra-nanocrystalline diamond substrates for high-performance photodetector with excellent UV light to dark current ratios. *Adv. Mater. Interfaces* 7, 1901694.
- Hu, H., Liu, Y., Han, G., Fang, C., Zhang, Y., Liu, H., Wang, Y., Liu, Y., Ye, J., Hao, Y., 2020. Effects of post annealing on electrical performance of polycrystalline Ga₂O₃ photodetector on sapphire. *Nanoscale Res. Lett.* 15, 100.
- Inamdar, S.I., Rajpure, K.Y., 2014. High-performance metal-semiconductor-metal UV photodetector based on spray deposited ZnO thin films. *J. Alloys Compd.* 595, 55–59.
- Ismail, R.A., Mousa, A.M., Shaker, S.S., 2019. Preparation of visible-enhanced PbI₂/MgO/Si heterojunction photodetector. *Optik* 202, 163585.
- Jain, R.K., Khanna, A., Gautam, Y.K., Singh, B.P., 2021. Sputter deposited crystalline V₂O₅, WO₃ and WO₃/V₂O₅ multi-layers for optical and electrochemical applications. *Appl. Surf. Sci.* 536, 147804.
- Jeong, H., Song, J.H., Jeong, S., Chang, W.S., 2020. Graphene/PbS quantum dot hybrid structure for application in near-infrared photodetectors. *Sci. Rep.* 10, 12475.
- Keuleyan, S., Lhuillier, E., Brajuskovic, V., Sionnest, P.G., 2011. Mid-infrared HgTe colloidal quantum dot photodetectors. *Nat. Photonics* 5, 489–493.
- Khan, H.R., Akram, B., Aamir, M., Malik, M.A., Tahir, A.A., Choudhary, M.A., Akhtar, J., 2020. Electronic tuning of zinc oxide by direct fabrication of chromium (Cr) incorporated photoanodes for visible-light driven water splitting applications. *Sci. Rep.* 10, 9707.
- Khomutov, G.B., Kislov, V.V., Antipina, M.N., Gainutdinov, R.V., Gubin, S.P., Obydenov, A.Y., Pavlov, S.A., Rakhyanskaya, A.A., Cherenkov, A.N.S., Soldatov, E.S., Suyatin, D.B., Tolstikhina, A.L., Trifonov, A.S., Yurova, T.V., 2003. Interfacial nanofabrication strategies in development of new functional nanomaterials and planar supra molecular nanostructures for nanoelectronics and nanotechnology. *Microelectron. Eng.* 69, 373–383.
- Kim, E.T., Madhukar, A., Ye, Z., Campbell, J.C., 2004. High detectivity InAs quantum dot infrared photodetectors. *Appl. Phys. Lett.* 84, 3277–3279.
- Konstantatos, G., Clifford, J., Levina, L., Sargent, E.H., 2007. Sensitive solution-processed visible-wavelength photodetectors. *Nat. Photonics* 1, 531–534.
- Konstantatos, G., Sargent, E.H., 2010. Nanostructured materials for photon detection. *Nat. Nanotechnol.* 5, 391–400.
- Konstantatos, G., Badioli, M., Gaudreau, L., Osmond, J., Bernechea, M., De Arquer, F.P.G., Gatti, F., Koppens, F.H.L., 2012. Hybrid graphene quantum dot phototransistors with ultrahigh gain. *Nat. Nanotechnol.* 7, 363–368.
- Kment, S., Krysova, H., Hubicka, Z., Kmentova, H., Kavan, L., Zboril, R., 2017. Very thin thermally stable TiO₂ blocking layers with enhanced electron transfer for solar cells. *Appl. Mater. Today* 9, 122–129.
- Laurienti, M., Lamberti, A., Gennchi, G.G., Roppolo, I., Canavese, G., Vitale-Brovarone, C., Ciolfani, G., Cauda, V., 2019. Graphene oxide finely tunes the bioactivity and drug delivery of mesoporous ZnO scaffolds. *ACS Appl. Mater. Interfaces* 11, 449–456.
- Lee, H.-Y., Lin, T.-S., Lee, C.-T., 2018. Stacked WO₃ nanosphere and WO₃ thin film metal-semiconductors-metal ultraviolet photodetectors. *ECS J. Solid State Sci. Technol.* 7, 85–87.
- Levine, B.F., Zussman, A., Gunapala, S.D., Asom, M.T., Kuo, J.M., Hobson, W.S., 1992. Photoexcited escape probability, optical gain, and noise in quantum well infrared photodetectors. *J. Appl. Phys.* 72, 4429–4443.
- Li, C., Ma, Y., Xiao, Y., Shen, L., Ding, L., 2020. Advances in perovskite photodetectors. *Info* 2, 1247–1256.
- Lin, Q., Armin, A., Burn, P.L., Meredith, P., 2015. Filterless narrowband visible photodetectors. *Nat. Photonics* 9, 687–694.
- Liu, H.C., Gao, M., McCaffrey, J., Wasilewski, Z.R., Fafard, S., 2001. Quantum dot infrared photodetectors. *Appl. Phys. Lett.* 78, 79–81.
- Liu, J., Zhong, M., Li, J., Pan, A., Zhu, X., 2015. Few-layer WO₃ nanosheets for high-performance UV-photodetectors. *Mater. Lett.* 148, 184–187.
- Liu, Y., Ji, Z., Tang, Q., Jiang, L., Li, H., He, M., Hu, W., Zhang, D., Jiang, L., Wang, X., Wang, C., Liu, Y., Zhu, D., 2005. Particle-size control and patterning of a charge-transfer complex for nanoelectronics. *Adv. Mater.* 17, 2953–2957.
- Livache, C., Martinez, B., Gouget, N., Greboval, C., Qu, J., Chu, A., Royer, S., Ithurria, S., Silly, M.G., Dubertret, B., Lhuillier, E., 2019. A colloidal quantum dot infrared photodetector and its use for intraband detection. *Nat. Commun.* 10, 2125.
- Li, Z., Yuan, X., Fu, L., Peng, K., Wang, F., Fu, X., Caroff, P., White, T.P., Tan, H.H., Jagadish, C., 2015. Room temperature GaAsSb single nanowire infrared photodetectors. *Nanotechnology* 26, 445202.
- Lv, Y., Li, H., Coileain, C.O., Zhang, D., Heng, C., Chang, C.R., Hung, K.M., Cheng, H.H., Wu, H.C., 2020. Photoelectrical properties of graphene/doped GeSn vertical heterostructures. *RSC Adv.* 10, 20921–20927.
- Mathew, J., Sreeja, V.G., Subin, P.S., Anila, E.I., 2020. Investigations on the effects of rGO incorporation on the photosensitivity of (Cd:Zn)S nanocrystalline thin film-based visible photodetectors by hydrothermal synthesis. *J. Mater. Sci. Mater. Electron.* 31, 2523–2529.
- Minami, T., Nishi, Y., Miyata, T., 2013. High-efficiency Cu₂O-based heterojunction solar cells fabricated using a Ga₂O₃ thin film as n-type layer. *APEX* 6, 044101.
- Mu, C., Xiang, J., Liu, Z., 2017. Photodetectors based on sensitized two-dimensional transition metal dichalcogenides-A review. *J. Mater. Res.* 32, 4115–4131.
- Murata, T., Asahi, S., Sanguineti, S., Kita, T., 2020. Infrared photodetector sensitized by InAs quantum dots embedded near an Al_{0.3}Ga_{0.7}As/GaAs heterointerface. *Sci. Rep.* 10, 11628.
- Neto, A.H.C., Guinea, F., Peres, N.M.R., Novoselov, K.S., Geim, A.K., 2009. The electronic properties of graphene. *Rev. Mod. Phys.* 81, 109–162.
- Omnès, F., Monroy, E., Munoz, E., Reverchon, J.-L., 2007. Wide bandgap UV photodetectors: a short review of devices and applications. *Proc. SPIE* 6473, 64730E.
- Papageorgiou, D.G., Kinloch, I.A., Young, R.J., 2017. Mechanical properties of graphene and graphene-based nanocomposites. *Prog. Mater. Sci.* 90, 75–127.
- Pan, D., Towe, E., Kennerly, S., 1998. Normal-incidence intersubband (In, Ga)As/GaAs quantum dot infrared photodetectors. *Appl. Phys. Lett.* 73, 1937–1939.
- Pandey, V.K., Dixit, C.K., Shukla, G.P., Pandey, C.K., 2020. Study of surface morphology of TiO₂-SnO₂ nanocomposites. *Mater. Today Proc.* 24, 960–965.
- Patel, A.B., Chauhan, P., Machhi, H.K., Narayan, S., Sumesh, C.K., Patel, K.D., Soni, S.S., Jha, P.K., Solanki, G.K., Pathak, V.M., 2020. Transferrable thin film of ultrasonically exfoliated MoSe₂ nanocrystals for efficient visible-light photodetector. *Physica E* 119, 114019.
- Patrocinio, A.O.T., Paula, L.F., Paniago, R.M., Freitag, J., Bahnemann, D.W., 2014. Layer-by-layer TiO₂/WO₃ thin films as efficient photocatalytic self-cleaning surfaces. *ACS Appl. Mater. Interfaces* 6, 16859–16866.
- Pearton, S.J., Norton, D.P., Ip, K., Heo, Y.W., Steiner, T., 2003. Recent progress in processing and properties of ZnO. *Superlattice. Microst.* 34, 3–32.
- Ponraj, J.S., Xu, Z.Q., Dhanabalan, S.C., Mu, H., Wang, Y., Yuan, J., Li, P., Thakur, S., Ashrafi, M., McCoubrey, K., Zhang, Y., Li, S., Zhang, H., Bao, Q., 2016. Photonics and optoelectronics of two-dimensional materials beyond graphene. *Nano-technology* 27, 462001.
- Qiao, K., Deng, H., Yang, X., Dong, D., Li, M., Hu, L., Liu, H., Song, H., Tang, J., 2016. Spectra-selective PbS quantum dot infrared photodetectors. *Nanoscale* 8, 7137–7143.
- Rabani, I., Lee, S.H., Kim, H.S., Yoo, J., Park, Y.R., Maqbool, T., Bathula, C., Jamil, Y., Hussain, S., Seo, Y.S., 2021. Suppressed photocatalytic activity of ZnO based Core@Shell and RCore@Shell nanostructure incorporated in the cellulose nanofiber. *Chemosphere* 269, 129311.
- Ramarajan, R., Kovendhan, M., Thangaraju, K., Joseph, D.P., Babu, R.R., Elumalai, V., 2020. Enhanced optical transparency and electrical conductivity of Ba and Sb co-doped SnO₂ thin films. *J. Alloys Compd.* 823, 153709.
- Ramasamy, P., Lim, D.H., Kim, B., Lee, S.H., Lee, M.S., Lee, J.S., 2016. All-inorganic cesium lead halide perovskite nanocrystals for photodetector applications. *Chem. Commun.* 52, 2067–2070.
- Ramiro, I., Ozdemir, O., Christodoulou, S., Gupta, S., Dalmases, M., Torre, I., Konstantatos, G., 2020. Mid- and long-wave infrared optoelectronics via

- intraband transitions in PbS colloidal quantum dots. *Nano Lett.* 20, 1003–1008.
- Reddy, Y.A.K., Ajitha, B., Sreedhar, A., Varlla, E., 2019a. Enhanced UV photodetector performance in bi-layer TiO₂/WO₃ sputtered films. *Appl. Surf. Sci.* 494, 575–582.
- Reddy, Y.A.K., Ajitha, B., Reddeppa, M., Sreedhar, A., 2019b. Improvement of UV photodetector properties of reactively sputtered TiO_{2-x} films through vacuum annealing. *J. Mater. Sci. Mater. Electron.* 30, 20687–20695.
- Ren, L., Tian, T., Li, Y., Huang, J., Zhao, X., 2013. High-performance UV photodetection of unique ZnO nanowires from zinc carbonate hydroxide nanobelts. *ACS Appl. Mater. Interfaces* 5, 5861–5867.
- Rodriguez, E., Mottaghizadeh, A., Gacemi, D., Palaferri, D., Asghari, Z., Jeannin, M., Vasanelli, A., Bigoli, A., Todorov, Y., Beck, M., Faist, J., Wang, Q.J., Sirtori, C., 2018. Room-temperature, wide-band, quantum well infrared photodetector for microwave optical links at 4.9 μm wavelength. *ACS Photonics* 5, 3689–3694.
- Rogalski, A., 2005. HgCdTe infrared detector material: history, status and outlook. *Rep. Prog. Phys.* 68, 2267–2336.
- Sankaranarayanan, S., Kandasamy, P., Raju, R., Krishnan, B., 2020. Fabrication of gallium nitride and nitrogen doped single layer graphene hybrid heterostructures for high performance photodetectors. *Sci. Rep.* 10, 14507.
- Saric, A., Despotovic, I., Stefanic, G., 2019. Alcoholic solvent influence on ZnO synthesis: a joint experimental and theoretical study. *J. Phys. Chem. C* 123, 29394–29407.
- Shaikh, S.K., Inamdar, S.I., Ganavle, V.V., Rajpure, K.Y., 2016. Chemical bath deposited ZnO thin film based UV photoconductive detector. *J. Alloys Compd.* 664, 242–249.
- Shewale, P.S., Lee, N.K., Lee, S.H., Kang, K.Y., Yu, Y.S., 2015. Ti doped ZnO thin film based UV photodetector: fabrication and characterization. *J. Alloys Compd.* 624, 251–257.
- Sharma, N., Ashraf, I.M., Khan, M.T., Shkir, M., Hamdy, M.S., Singh, A., Almohammed, A., Ahmed, F.B.M., Yahia, I.S., Alfaify, S., 2020. Enhancement in photodetection properties of PbI₂ with graphene oxide doping for visible-light photodetectors. *Sens. Actuators, A* 314, 112223.
- Shi, L., Nihtianov, S., Member, S., 2016. Comparative study of silicon-based ultraviolet comparative study of silicon-based ultraviolet photodetectors. *IEEE Sensor. J.* 12, 2453–2459.
- Shiau, J.S., Brahma, S., Huang, J.L., Liu, C.P., 2020. Fabrication of flexible UV-B photodetectors made of Mg_xZn_{1-x}O films on PI substrate for enhanced sensitivity by piezophotronic Effect. *Appl. Mater. Today* 20, 100705.
- Shkir, M., Khan, M.T., Ashraf, I.M., Almohammed, A., Dieguez, E., Alfaify, S., 2019. High-performance visible light photodetectors based on inorganic CZT and InCZT single crystals. *Sci. Rep.* 9, 12436.
- Siciliano, T., Tepore, A., Micocci, G., Serra, A., Manno, D., Filippo, E., 2008. WO₃ gas sensors prepared by thermal oxidation of tungsten. *Sens. Actuators, B* 133, 321–326.
- Siontas, S., Li, D., Wang, H., Aravind, A.V.P.S., Zaslavsky, A., Pacifici, D., 2019. High-performance germanium quantum dot photodetectors in the visible and near infrared. *Mater. Sci. Semicond. Process.* 92, 19–27.
- Sun, Z., Liu, Z., Li, J., Tai, G., Lau, S.P., Yan, F., 2012. Infrared photodetectors based on CVD-grown graphene and PbS quantum dots with ultrahigh responsivity. *Adv. Mater.* 24, 5878–5883.
- Tang, W., Zhou, J., Zheng, Y., Zhou, Y., Hao, J., Chen, X., Lu, W., 2018. All-dielectric resonant waveguide based quantum well infrared photodetectors for hyperspectral detection. *Opt. Commun.* 427, 196–201.
- Tang, Y., Fang, H., Long, M., Chen, G., Zheng, Z., Zhang, J., Zhou, W., Ning, Z., Zhu, Z., Feng, Y., Qin, S., Chen, X., Lu, W., Hu, W., 2018. Significant enhancement of single-walled carbon nanotube based infrared photodetector using PbS quantum dots. *IEEE J. Sel. Top. Quant. Electron.* 24, 1–8.
- Tas, H., Sahin, M., 2012. The inter-sublevel optical properties of a spherical quantum dot-quantum well with and without a donor impurity. *J. Appl. Phys.* 112, 053717.
- Tezcan, D.S., Eminoglu, S., Akin, T., 2003. A low-cost uncooled infrared microbolometer detector in standard CMOS technology. *IEEE Trans. Electron. Dev.* 50, 494–502.
- Tian, W., Lu, H., Li, L., 2015. Nanoscale ultraviolet photodetectors based on one dimensional metal oxide nanostructures. *Nano Res.* 8, 382–405.
- Tian, W., Zhang, C., Zhai, T., Li, S.L., Wang, X., Liao, M., Tsukagoshi, K., Golberg, D., Bando, Y., 2013. Flexible SnO₂ hollow nanosphere film based high-performance ultraviolet photodetector. *Chem. Commun.* 49, 3739–3741.
- Tran, H., Pham, T., Margetis, J., Zhou, Y., Dou, W., Grant, P.C., Grant, J.M., Kabi, S.A., Sun, G., Soref, R.A., Tolle, J., Zhang, Y.H., Du, W., Li, B., Mortazavi, M., Yu, S.Q., 2019. Si-based GeSn photodetectors toward mid-infrared imaging applications. *ACS Photonics* 6, 2807–2815.
- Velusamy, D.B., Kim, R.H., Cha, S., Huh, J., Khazaeinezhad, R., Kassani, S.H., Song, G., Cho, S.M., Cho, S.H., Hwang, I., Lee, J., Oh, K., Cho, H., Park, C., 2015. Flexible transition metal dichalcogenide nanosheets for band-selective photodetection. *Nat. Commun.* 6, 8063.
- Wang, B., Zhong, S.P., Zhang, Z., Bin, Zheng, Z.Q., Zhang, Y.P., Zhang, H., 2019. Broadband photodetectors based on 2D group IV_A metal chalcogenides semiconductors. *Appl. Mater. Today* 15, 115–138.
- Wang, L., Jie, J., Shao, Z., Zhang, Q., Zhang, X., Wang, Y., Sun, Z., Lee, S.T., 2015. MoS₂/Si heterojunction with vertically standing layered structure for ultrafast, high-detectivity, self-driven visible-near infrared photodetectors. *Adv. Funct. Mater.* 25, 2910–2919.
- Wang, Y., Gan, L., Chen, J., Yang, R., Zhai, T., 2017. Achieving highly uniform two-dimensional PbI₂ flakes for photodetectors via space confined physical vapor deposition. *Sci. Bull.* 62, 1654–1662.
- Wang, Y., Zhang, X.W., Jiang, Q., Liu, H., Wang, D., Meng, J., You, J., Yin, Z., 2018. Interface engineering of high-performance perovskite photodetectors based on PVP/SnO₂ electron transport layer. *ACS Appl. Mater. Interfaces* 3, 13227–13238.
- Wang, H., Liu, J.L., Wu, X.X., Zhang, S.Q., Zhang, Z.K., Pan, W.W., Yuan, G., Yuan, C.L., Ren, Y.L., Lei, W., 2020b. Ultra-long high quality catalyst-free WO₃ nanowires for fabricating high-performance visible photodetectors. *Nanotechnology* 31, 274003.
- Wang, Y., Song, L., Chen, Y., Huang, W., 2020a. Emerging new-generation photodetectors based on lowdimensional halide perovskites. *ACS Photonics* 7, 10–28.
- Wang, Z., Yu, R., Wen, X., Liu, Y., Pan, C., Wu, W., Wang, Z.L., 2014. Optimizing performance of silicon-based p-n junction photodetectors by the piezophototronic effect. *ACS Nano* 8, 12866–12873.
- Wang, Z.L., 2007. Novel nanostructures of ZnO for nanoscale photonics, optoelectronics, piezoelectricity, and sensing. *Appl. Phys. Mater. Process.* 88, 7–15.
- Wei, Q., Shen, B., Chen, Y., Xu, B., Xia, Y., Yin, J., Liu, Z., 2017. Large-sized PbI₂ single crystal grown by co-solvent method for visible-light photo-detector application. *Mater. Lett.* 193, 101–104.
- Wen, Y., Wang, Q., Yin, L., Liu, Q., Wang, F., Wang, F., Wang, Z., Liu, K., Xu, K., Huang, Y., Shifa, T.A., Jiang, C., Xiong, J., He, J., 2016. Epitaxial 2D PbS nanoplates arrays with highly efficient infrared response. *Adv. Mater.* 28, 8051–8057.
- Wu, J., Jiang, Q., Chen, S., Tang, M., Mazur, Y.I., Maidaniuk, Y., Benamarra, M., Semtsiv, M.P., Masselink, W.T., Sablon, K.A., Salamo, G.J., Liu, H., 2016b. Monolithically integrated InAs/GaAs quantum dot mid-infrared photodetectors on silicon substrates. *ACS Photonics* 3, 749–753.
- Wu, G., Wang, X., Wang, P., Huang, H., Chen, Y., Sun, S., Shen, H., Lin, T., Wang, J., Zhang, S., Bian, L., Sun, J., Meng, X., Chu, J., 2016a. Visible to short wavelength infrared In₂Se₃-nanoflake photodetector gated by a ferroelectric polymer. *Nanotechnology* 27, 364002.
- Wu, D.H., Zhang, Y.Y., Razeghi, M., 2018. Room temperature operation of In_xGa_{1-x}Sb/InAs type-II quantum well infrared photodetectors grown by MOCVD. *Appl. Phys. Lett.* 112, 111103.
- Xia, Y., Rogers, J.A., Paul, K.E., Whitesides, G.M., 1999. Unconventional methods for fabricating and patterning nanostructures. *Chem. Rev.* 99, 1823–1848.
- Xie, C., Fusino, V., Khalid, A., Steer, M.J., Sorel, M., Thayne, I.G., Cumming, D.R.S., 2015. Monolithic integration of an active InSb-based mid-infrared photopixel with a GaAs MESFET. *IEEE Trans. Electron. Dev.* 62, 4069–4075.
- Xing, J., Wei, H., Guo, E.J., Yang, F., 2011. Highly sensitive fast-response UV photodetectors based on epitaxial TiO₂ films. *J. Phys. D Appl. Phys.* 44, 375104.
- Xu, B., Zhou, J.L., Altaee, A., Ahmed, M.B., Johir, M.A.H., Ren, J., Li, X., 2020. Improved photocatalysis of perfluorooctanoic acid in water and wastewater by Ga₂O₃/UV system assisted by peroxymonosulfate. *Chemosphere* 239, 124722.
- Xue, D.J., Wang, J.J., Wang, Y.Q., Xin, S., Guo, Y.G., Wan, L.J., 2011. Facile synthesis of germanium nanocrystals and their application in organic-inorganic hybrid photodetectors. *Adv. Mater.* 23, 3704–3707.
- Xue, H., Kong, X., Liu, Z., Liu, C., Zhou, J., Chen, W., Ruan, S., Xu, Q., 2007. TiO₂ based metal-semiconductor-metal ultraviolet photodetectors. *Appl. Phys. Lett.* 90, 201118.
- Yadav, P.V.K., Reddy, Y.A.K., Ajitha, B., Minnam Reddy, V.R., 2019. Oxygen partial pressure dependent UV photodetector performance of WO₃ sputtered thin films. *J. Alloys Compd.* 816, 152565.
- Yadav, P.V.K., Ajitha, B., Reddy, Y.A.K., Minnam Reddy, V.R., Reddeppa, M., Kim, M.D., 2021. Effect of sputter pressure on UV photodetector performance of WO₃ thin films. *Appl. Surf. Sci.* 536, 147947.
- Yang, F., Cong, H., Yu, K., Zhou, L., Wang, N., Liu, Z., Li, C., Wang, Q., Cheng, B., 2017. Ultrathin broadband germanium-graphene hybrid photodetector with high performance. *ACS Appl. Mater. Interfaces* 9, 13422–13429.
- Yang, W., Hu, K., Teng, F., Weng, J., Zhang, Y., Fang, X., 2018. High-performance silicon-compatible large-area UV-to-visible broadband photodetector based on integrated lattice-matched type II Se/n-Si heterojunctions. *Nano Lett.* 18, 4697–4703.
- Yan, L., Yu, J., Luo, H., 2017. Ultrafine TiO₂ nanoparticles on reduced graphene oxide as anode materials for lithium ion batteries. *Appl. Mater. Today* 8, 31–34.
- Yamada, N., Kondo, Y., Cao, X., Nakano, Y., 2019. Visible-blind wide-dynamic-range fast-response self-powered ultraviolet photodetector based on CuI/In-Ga-Zn-O heterojunction. *Appl. Mater. Today* 15, 153–162.
- Ye, Z., Campbell, J.C., Chen, Z., Kim, E.T., Madhukar, A., 2002. InAs quantum dot infrared photodetectors with In_{0.15}Ga_{0.85}As strain-relief cap layers. *J. Appl. Phys.* 92, 7462.
- Yuan, Y., Zhang, X., Liu, H., Yang, T., Zheng, W., Zheng, B., Jiang, F., Li, L., Li, D., Zhu, X., Pan, A., 2019. Growth of CdSe/MoS₂ vertical heterostructures for fast visible-wavelength photodetectors. *J. Alloys Compd.* 815, 152309.
- Zeng, H., Du, X.W., Singh, S.C., Kulнич, S.A., Yang, S., He, J., Cai, W., 2012. Nanomaterials via laser ablation/irradiation in liquid: a review. *Adv. Funct. Mater.* 22, 1333–1353.
- Zhai, T., Fang, X., Liao, M., Xu, X., Zeng, H., Yoshio, B., Golberg, D., 2009. A comprehensive review of one-dimensional metal-oxide nanostructure photodetectors. *Sensors* 9, 6504–6529.
- Zhang, D., Du, Z., Ma, M., Zheng, W., Liu, S., Huang, F., 2019. Enhanced performance of solar-blind ultraviolet photodetector based on Mg-doped amorphous gallium oxide film. *Vacuum* 159, 204–208.
- Zhang, Y., Huang, P., Guo, J., Shi, R., Huang, W., Shi, Z., Wu, L., Zhang, F., Gao, L., Li, C., Zhang, X., Xu, J., Zhang, H., 2020. Graphdiyne-based flexible photodetectors with high responsivity and detectivity. *Adv. Mater.* 32, 2001082.
- Zhang, Y., Yu, Y., Mi, L., Wang, H., Zhu, Z., Wu, Q., Zhang, Y., Jiang, Y., 2016. In situ fabrication of vertical multilayered MoS₂/Si homotype heterojunction for high-

- speed visible-near-infrared photodetectors. *Small* 12, 1062–1071.
- Zhang, Y., Wang, C., 2020. Environment-friendly synthesis of carbon-encapsulated SnO₂ Core-shell nanocubes as high-performance anode materials for lithium ion batteries. *Mater. Today Energy* 16, 100406.
- Zhang, Z., Wong, L.M., Zhang, Z., Wu, Z., Wang, S., Chi, D., Hong, R., Yang, W., 2015. Pulse laser deposition of epitaxial TiO₂ thin films for high-performance ultraviolet photodetectors. *Appl. Surf. Sci.* 355, 398–402.
- Zhao, Y., Li, C., Liu, X., Gu, F., Jiang, H., Shao, W., Zhang, L., He, Y., 2007. Synthesis and optical properties of TiO₂ nanoparticles. *Mater. Lett.* 61, 79–83.
- Zhao, Y., Li, L., Liu, S., Wang, J., Xu, J., Shi, Y., Chen, K., Cabarrocas, P.R.I., Yu, L., 2020. Germanium quantum dot infrared photodetectors addressed by self-aligned silicon nanowire electrodes. *Nanotechnology* 31, 145602.
- Zheng, L., Yu, P., Hu, K., Teng, F., Chen, H., Fang, X., 2016. Scalable-production, self-powered TiO₂ nanowell-organic hybrid uv photodetectors with tunable performances. *ACS Appl. Mater. Interfaces* 8, 33924–33932.
- Zhong, M., Wei, Z., Meng, X., Wu, F., Li, J., 2015. High-performance single crystalline UV photodetectors of β -Ga₂O₃. *J. Alloys Compd.* 619, 572–575.
- Zhu, D.D., Xia, J., Wang, L., Li, X.Z., Tian, L.F., Meng, X.M., 2016. Van der Waals epitaxy and photoresponse of two-dimensional CdSe plates. *Nanoscale* 8, 11375–11379.
- Zeng, L.H., Wang, M.Z., Hu, H., Nie, B., Yu, Y.Q., Wu, C.Y., Wang, L., Hu, J.G., Xie, C., Liang, F.X., Luo, L.B., 2013. Monolayer graphene/germanium Schottky junction as high-performance self-driven infrared light photodetector. *ACS Appl. Mater. Interfaces* 5, 9362–9366.
- Zhu, W., Deng, M., Chen, D., Zhang, Z., Chai, W., Chen, D., Xi, H., Zhang, J., Zhang, C., Hao, Y., 2020a. Dual-phase CsPbCl₃-Cs₄PbCl₆ perovskite films for self-powered, visible-blind UV photodetectors with fast response. *ACS Appl. Mater. Interfaces* 12, 32961–32969.
- Zhu, W., Xiong, L., Si, J., Hu, Z., Gao, X., Long, L., Li, T., Wan, R., Zhang, L., Wang, L., 2020b. Influence of deposition temperature on amorphous Ga₂O₃ solar-blind ultraviolet photodetector. *Semicond. Sci. Technol.* 35, 055037.